Title
Direct Synthesis of Semiconducting Transition Metal Dichalcogenide Monolayers and Heterojunctions by Chemical Vapor Deposition

Author
Shaw, Jonathan Caplette

Publication Date
2016

Peer reviewed|Thesis/dissertation

UNIVERSITY OF CALIFORNIA

Los Angeles

Direct Synthesis of Semiconducting Transition Metal Dichalcogenide Monolayers and Heterojunctions by Chemical Vapor Deposition

A dissertation submitted in partial satisfaction of the

requirements for the degree Doctor of Philosophy

in Chemistry

by

Jonathan Caplette Shaw

2016

ABSTRACT OF THE DISSERTATION

Direct Synthesis of Semiconducting Transition Metal Dichalcogenide Monolayers and Heterojunctions by Chemical Vapor Deposition

by

Jonathan Caplette Shaw

Doctor of Philosophy in Chemistry

University of California, Los Angeles, 2016

Professor Xiangfeng Duan, Chair

Since the isolation of graphene in 2004, interest regarding two-dimensional materials properties and their synthesis has exploded. Group VIb transition metal dichalcogenides (MX_2: M=Mo, W; X = S, Se) are a class of layered semiconductors that show unique layer-number dependent electronic and optical properties. For example, bulk three-dimensional MoS_2 is an indirect band gap semiconductor with a 1.2 eV band gap, while monolayer MoS_2 nanohseet is a direct band gap semiconductor with a 1.8 eV energy gap. This exciting change in electronic structure opens several possibilities towards implementing these materials in novel device assemblies such as field effect transistors, electroluminescent devices, and flexible optoelectronic devices. While these materials offer great promise, isolating transition metal dichalcogenide monolayers requires tedious mechanical exfoliations using scotch tape, which is neither practical nor scalable for production. In the first part of my dissertation, we investigated the synthesis of MoS_2 and

WS_2 monolayers using chemical vapor deposition. The isolated nanosheets were single crystal, triangular, and had edge lengths up to 100 μm. In the next chapter, by utilizing H_2 gas in a chemical vapor deposition apparatus, $MoSe_2$ monolayers and few-layers were also synthesized. The $MoSe_2$ nanosheets exhibited thickness-dependent vibrational and optical properties, and a notable intense photoluminescence emission from the direct band gap monolayer region. In the following chapter, we describe an alternative method to produce WSe_2 nanosheets by physically vaporizing of WSe_2 powder at a high temperature. Using WSe_2 powder directly is advantageous since under optimal conditions we can selectively grow single-layer WSe_2 domains or single-layer films up to several square centimeters. Lastly, we combine the synthesis of the transition metal chalcogenides previously described into lateral and vertical heterostructures grown *in situ* by chemical vapor deposition. The lateral MoS_2-$MoSe_2$ and WS_2-WSe_2 heterostructures formed stitched monolayer heterojunctions confirmed, as confirmed by photoluminescence and Raman spectroscopy studies. Vertical MoS_2-$MoSe_2$ and WS_2-WSe_2 heterojunctions were two layers thick and had vibrational and emission confirmations of their composition. This dissertation lays the foundation for the rational synthesis of two-dimensional transition metal dichalcogenide monolayer and heterostructure, which represents the key challenge to apply these exciting materials systems into functional optoelectronic devices.

The dissertation of Jonathan Caplette Shaw is approved.

Richard B. Kaner

Yu Huang

Xiangfeng Duan, Committee Chair

University of California, Los Angeles

2016

Dedicated to my parents, for their unwavering support,

to my brother Ben, for his spirit,

and to Minh, for her encouragement

Table of Contents

List of Figures

Acknowledgements

First and foremost, I'd like to thank my adviser, Professor Xiangfeng Duan for guiding me throughout my tenancy at UCLA. Professor Duan gave me an opportunity to work in his group in June 2011 and for that I will always be grateful. Since 2011, Professor Duan has helped shape me into a dutiful researcher by engaging with me in fruitful scientific discussions, providing sincere encouragement, and constructive criticism. When I first started working in Professor Duan's group, he assigned me to train under experienced graduate students and post docs with extensive technical and academic knowledge in nanotechnology and chemical vapor deposition. I would also like to thank my committee members Professor Yu Huang, Professor Richard B. Kaner, and Professor William Gelbart.

Since 2011, numerous graduate students and post docs from Professor Duan and Professor Yu Huang's group have contributed to my achievements in graduate school. There are a few notable individuals that have been especially helpful that I would like to mention. Dr. Xing Zhong was my first mentor in graduate school, and taught me the basic way to approach scientific research. Dr. Hua Zhang worked with me from 2011 to 2012, as we had collaborated on a successful project battery together (along with Xing Zhong). Dr. Hailong Zhou and I collaborated extensively from 2011 to 2014. Hailong taught me the basics of chemical vapor deposition reactions and equipment, and the completion of my projects couldn't have been completed without his help.

VITA

2004	High School Diploma Willow Glen High School San Jose, California
2005-2008	Attended De Anza College Cupertino, California
2011	Bachelor of Science in Chemistry University of California, Los Angeles Los Angeles, California
2012	Masters of Science in Chemistry University of California, Los Angeles Los Angeles, California
2014	Faculty Award For Innovation in Inorganic Chemistry
Expected in 2016	Doctor of Philosophy in Chemistry University of California, Los Angeles Los Angeles, California

Chapter 1. Introduction to two-dimensional materials: properties and synthesis

1.1 The rise of two-dimensional nanomaterials

Nanoscience constitutes the physical, chemical, and biological properties and applications and creation of materials in the nanoscale.[1] A nanomaterial is defined as any material having dimensions or planes on the order of 1 to 100 nm.[1] Classes of nanomaterials can be broken down into three distinctions: zero-dimensional (0-D), one-dimensional (1-D), and two-dimensional (2-D). In a 0-D material, no aspect ratio exists but the diameter of the nanoparticles is less than 100 nm (typically on the order of 1-10) nm. 0-D materials have an aspect ratios of (x:y:z) = 1:1:1. Common examples include CdS or CdSe semiconducting nanocrystals, Pt or bimetallic nanoparticles for catalysis, and C_{60} buckminsterfullerenes.[2-6] 1-D materials have extended spans in one direction, but nanoscale proportions all others. 1-D materials typically have aspect ratios of (x:y:z) = 1:1:100, in which the material is extended but lacks width, such as a wire. Semiconducting Si, SiGe, GaAs, or InP nanowires, metallic Pt or Au nanowires, and carbon nanotubes are recognized and well-studied 1-D materials.[7-11] A 2-D material can be described as a layered crystal, which has a thickness on the scale of several nanometers and lateral lengths in the micron scale and beyond. 2-D materials typically have an aspect ratio of (x:y:z) = (100:100:1), in which the material has an extended blanket or sheet like structure, but is very thin (typically one or two atoms thick). To summarize, the class of the nanomaterial is defined by its aspect ratio or the proportional relationship between a material's length, width or diameter, and thickness.

To understand how to isolate a 2D sheet, one must first understand the bulk 3D counterpart. This can be clearly demonstrated by a layered crystal of graphite, as it is both naturally occurring and has been extensively studied. Within the planes of the graphite layers, the

crystals are held together by strong, covalent bonds produced by sp^2 hybridized molecular orbitals.[12] The p-orbitals perpendicular to the sp_2 bonds, form π-π bonds which are delocalized over the entire sheet to give graphite its metallic condictivity.[12] All of the aforementioned properties are confined within the plane of the layer, which constitutes a single "sheet." Each of these sheets is held in place by weak van der Waals forces from the layers above and below. Van der Waals bonds are significantly weaker than covalent bonds[12] and can easily slide when mild force is applied, making graphite a useful writing utensil or solid-state lubricant.[13] If a single sheet of graphite is isolated, the geometry is shifted from a 3-D crystal to a 2-D crystal. In 3-D space (x:y:z), a 2-D crystal has dimensions in the x and y directions, but not in the z direction. Separating single-sheets results in an isolated 2-D product. Figure 1.1 illustrates classes of nanomaterials using sp^2-hybridized carbon as an example.

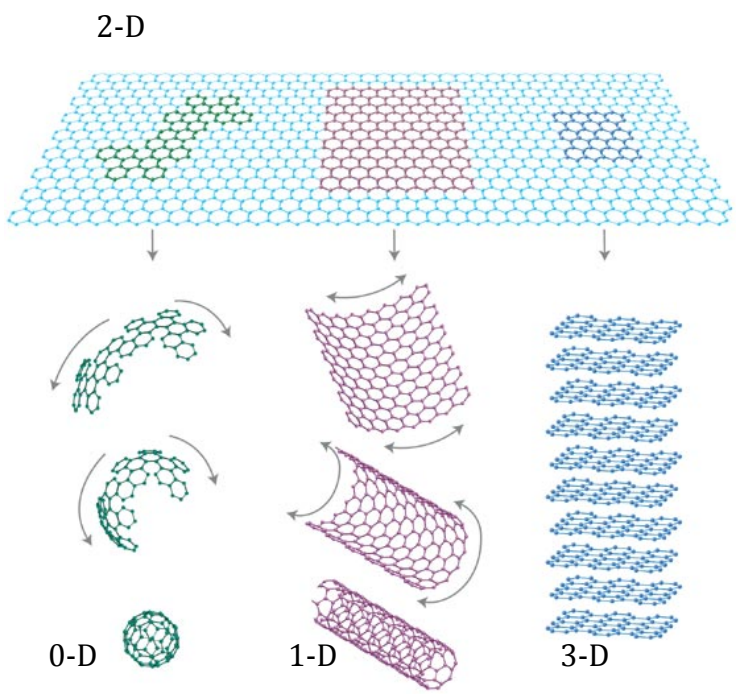

Figure 1.1 Four allotropes of sp^2 carbon. Graphene (2-D) can be rolled up into a C_{60} buckyball (0-D), a nanotube (1-D), or stacked to create graphite (3-D). Reprinted by permission from Macmillian Publishers Ltd: Nature Materials[55], **2007**.

Theoretical studies predicted single isolated sheets of graphite to be unstable and therefore impossible to isolate.[14] In 2004, experimental physicists A. K. Geim and K. S. Novoselov isolated and observed a single atomic layer sheet of carbon, which was coined graphene.[15] Geim and Novoselov isolated graphene using a top-down mechanical exfoliation approach with scotch tape and were awarded the Nobel Prize in Physics in 2010 for their discovery. Graphene has exceptional physical properties, including an extremely high-electron mobility, highest thermal conductivity, highest mechanical strength and flexibility, optical transparency, and an ultra-thin 2-D geometry .[16-20] With these advantageous properties, graphene continues to attract vast attention in an assortment of research areas including chemical synthesis, electronic device fabrication, and energy storage.[21-24] In addition, due to the ultra-fast mobility of graphene (up to 10^6 $cm^2/V\bullet s$), numerous electronic transistors and devices have been fabricated.[20,22] However, despite its advantages the electronic structure of graphene can be best described as a zero band gap semiconductor.[20] Since there is essentially no band gap, the device cannot be effectively shut off which results in leakage current.[20] To address these issues, other semiconducting 2-D materials have been studied.

1.2 Transition metal dichalcogenides

Essentially, hundreds of layered materials an their 2D counterparts exist, but for practical considerations only layered transition metal dichalcogenides (TMDs) will be considered for the remainder of this chapter. There are forty known TMD compounds.[25] The layered TMDs structure entails a transition metal center and chalcogen atoms (S, Se, Te) sandwiching the transition metal atoms.[26] Layered TMDs can be segregated by their periodic group; group four metals (Ti, Hf, Zr), group five metals (V, Nb, Ta), group six metals (Mo, W), group seven metals (Tc, Re), group nine metals (Co, Rh, Ir) and group ten metals (Pd, Pt) (Fig. 1.2a).[25] Layered

TMDs have a wide range of electronic properties including metallic, insulating and semiconducting.[25]

Perhaps the most well-known and broadly studied TMD belongs in group six: MoS_2, a naturally occurring mineral and chief ore for molybdenum metal refining.[27] MoS_2 has principally been utilized as a dry lubricant owing to its stability up to 350 °C under oxidizing conditions.[28] MoS_2 has also been employed as a desulfurization cocatalyst in the petroleum industry.[29] The original structural studies of MoS_2 determined the material to have a AA' stacked, 2-H hexagonal crystal structure with a $P6_3/mmc$ point group (Fig. 1.2 b,c).[25,26,30] The electronic properties of bulk MoS_2 is semiconducting with a 1.2 eV indirect band gap.[31] A single layer of MoS_2 can be best described as a Mo sheet sandwiched between two S chalcogen sheets, which is covalently bound to Mo atoms.[26] The unit cell of MoS_2 shows that the Mo atoms have a coordination of six, the sulfur atoms have a coordination of three and exists in a trigonal prismatic D_{3h} space group.[26] The trigonal prismatic D_{3h} space group differs from an Oh space group in that the S atoms in the unit cell are above and below. In an O_h system, the S atoms have "i," or inversion symmetry (S atom at [x,y,z] and [-x,-y,-z]). It's worth mentioning that MoS_2 has a corresponding O_h allotrope, but the material is metastable and will not be mentioned again in this thesis.

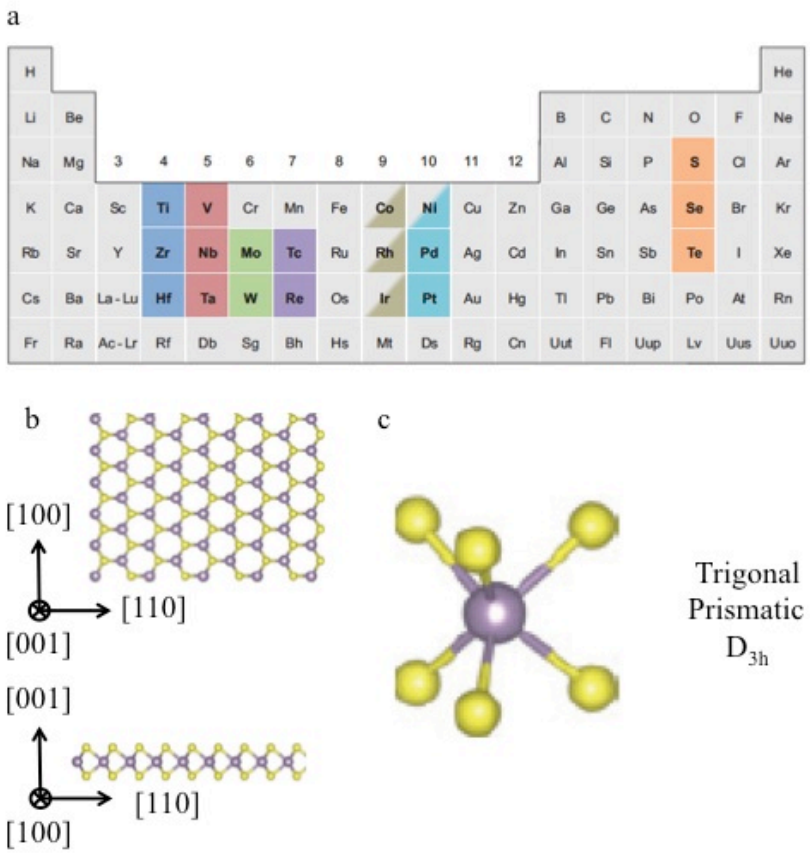

Figure 1.2 (a) Periodic table highlighting the transition metals and chalcogenides, which combine to yield transition metal dichalcogenide compounds. Group 4, group 5, group 6, group 7, group 9 and group 10 transition metals are highlighted. **(b)** Crystal structure of group 6 transition metal dichalcogenides (MX_2: M = Mo, W; X = S, Se, Te); 2-H hexagonal trigonal prismatic crystal structure. A single layer is consists of a chalcogen sandwiching a metal atom. **(c)** A single molecular unit; D_{3h} trigonal prismatic unit. The metal atom (purple) is sandwiched by chalcogens (yellow). Adapted with permission from Macmillian Publishers Ltd: Nature Chemistry[25], **2013**.

The semiconducting nature of MoS_2 can be described by group theory and ligand field theory using trigonal prismatic MX_6 prisms as a model.[32] The bonding within the MoS_2 layer consists primarily of S_sS_p-Mo_dMo_s hybridization, and complete occupation of s and p S orbitals. The saturation of S bonds results in the inertness between the layers of MoS_2 along the basal plane.[26] For MoS_2 (and for all group six TMDs) the Mo has a formal charge of +4, while the S has a formal charge of -2. Consequently, two d-electrons remain on the Mo atom (d_2 configuration) (Fig. 1.3a). The valence band and lowest energy bonds consist of Mo-d/S-p

hybridized bonding states.[33] The next highest energy levels are essentially non-bonding states. Ligand field theory tells us that degenerate d-orbitals morph to lose symmetry in order to minimize the overall energy of the system.[12] The splitting in a trigional prismatic coordination results in d_z^2 orbitals having the lowest energy, followed by degenerate d_{xy} and $d_{x^2-y^2}$ orbitals, followed by highest energy d_{xz} and d_{yz}.[12] Focusing again on Mo, the two electrons left on Mo occupy the d_z^2 orbital, and thus have a energy barrier to the next lowest unoccupied state (Fig. 1.3b). This ligand field theory model also explains why V, Nb, Ta based TMDs are metallic (d_1 configuration.

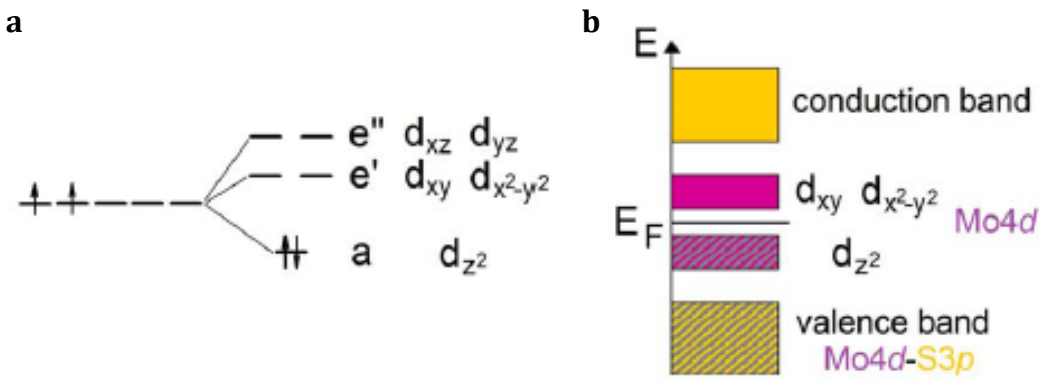

Figure 1.3 (a) Ligand field theory model for group six transition metal dichalcogenides (d_2) in which degenerate d-orbitals split in a trigonal prismatic orientation. **(b)** Resulting band structure showing the semiconducting gap between the d_z^2 and d_{xy}, $d_{x^2-y^2}$ orbitals. Image adapted from Ref. 26.

The ligand field theory model is an oversimplification, and a more accurate and empirical calculation is needed to accurately determine the bulk electronic structure. Calculations on the band structure reveal that close to the Γ-point, the valence band consists of a mixture of Mo d_{z2} and S p_z interactions (Fig 1.4).[34] Since these orbital interactions are primarily located in the out-of-plane direction, their energy varies heavily on interlayer distance. When the interlayer distance increases, in the case of separating a 2-D sheet, the energy of the valence bands decrease

due to the antibonding nature of these orbital interactions.[35] Alternatively, valence band maximum and conduction band minimum at the K-point do not change when the layers detach. The energy states at the K-point consist of Mo-Mo d_{xy} and $d_{dx^2-y^2}$ exchanges, within the plane of the MoS_2 sheet and independent of interlayer dynamics.[35] The gap between these two energy levels remains constant at 1.9 eV and doesn't require a change in momentum.[35] Therefore, when MoS_2 is thinned to a single 2-D sheet, there is a shift in electronic structure from a 1.2 eV indirect band gap (Γ➔K) to a 1.8 eV direct band gap (K➔K).

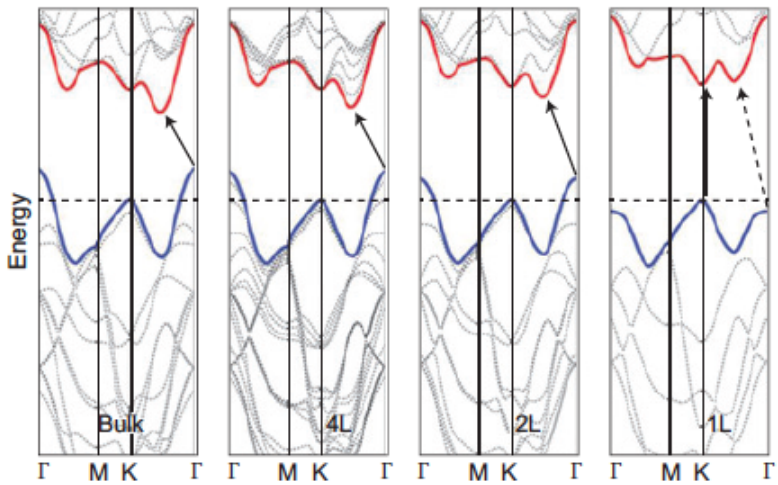

Figure 1.4 Energy dispersion (energy vs. momentum) in bulk, quadlayer, bilayer and monolayer MoS_2. The blue and red lines trace the valence band maximum and conduction band minimum, respectively. The electronic signature is primarily indirect except when confined to a monolayer. Reprinted with permission[34] © American Chemical Society.

The considerable shift from an indirect-to-direct band gap is a physical property that is shared with all group six TMDs (MX_2; M = Mo, W; X = S, Se, Te). In addition, the ability to shift from an indirect-to-direct band gap is a lucrative property, which has made 2-D TMD research a popular and innovative topic in the scientific community.[36] Direct band gap semiconductors are useful as they have several orders of magnitude larger quantum yield in absorption and emission of photons compared to an indirect band gap semiconductor. The

sizable direct band gap of 2-D TMDs (within visible and near-IR range) offers several advantages over traditional semiconductors. TMDs are atomically thin (less than one nm thick), flexible, transparent, can be prepared in sheets, are switchable between on and off states, and exhibit chemical inertness.[36] Thin, flexible and transparent optoelectronic devices are attractive for applications including solar arrays, wearable electronics, and transparent displays.[36] Mechanically exfoliated TMD samples have been successfully assembled into useful devices such as field effect transistors, photodetectors, electroluminescent devices, and chemical sensors.[37-40] Since 2007, research has been focused at the isolation, assembly, and preparation of MoS_2 and related TMDs into useful electronic and optoelectronic devices, all of which depend on the isolation of a single 2-D sheet.

1.3 Isolating two-dimensional transition metal dichalcogenide nanosheets

1.3.1 Top down methods

The mechanical cleavage method to isolate single-layers can be applied to TMDs and MoS_2. In principle, these mechanical exfoliation methods are simple. In 2005, K. S. Novoselov *et al*. isolated 2-D MoS_2 by rubbing a solid surface with a large 3-D crystal, similar to "using chalk on a blackboard."[41] The group found several flakes on the substrate, which were identified as single and few-layer MoS_2 crystals. 2-D TMDs produced using cleavage have been reported as the most crystalline and best quality among all methods reported. The simplicity of mechanical exfoliation and cleavage make it practical for physicists, chemists, and engineers to research fundamental properties and fabricate devices.

Chemical exfoliation can also be employed to separate 3-D TMD layers into their 2-D counterparts. This method utilizes chemical intercalation to weaken the interaction between the atomic layers. Coleman *et al.* exfoliated MoS_2, WS_2, $MoSe_2$ and $MoTe_2$ in (N)-methyl-

pyrrolidone (NMP) and isopropanol (IPA) by sonication. The single and few-layers obtained had lateral dimensions from 50 nm to 1 μm.[42] Controllable lithium intercalation is also an alternative method which yields single-layer nanosheets.[43] Lithium intercalation acts via two mechanisms. First, lithium weakens the van der Waals forces between the layers, making the separation easier. Second, Li is oxidized to Li^{+1}, which reduces water, produces H_2, and forces the layers apart.[43]

Laser and plasma thinning are other top-down methods which can yield single-layer MoS_2. Castellanos-Gomize *et al*. fabricated a user-defined size and shape monolayer MoS_2 sheet with a laser. The optoelectronic signature was comparable to pristine MoS_2.[44] Liu *et al*. developed a process to thin MoS_2 using an Ar Plasma which allowed the authors to control the entire sheet thickness, as well as fabricate bilayers monolayers and bilayers within the same nanosheet.[45]

While strong contributions to the field have been made, to date top down methods have been neither scalable nor ideal for the mass fabrication of MoS_2 single layers and sheets. Mechanical exfoliations using scotch tape yield pristine MoS_2 nanosheets, unmatched in both their crystallinity and performance. However, cleavage methods are tedious and are only realistic for basic research and proof of principle devices. Chemical exfoliations and intercalations are time and resource consuming, and do not have high enough yields to be industrially scalable. Laser thinning and plasma etching methods are promising, but the process has yet to be fully optimized. As an alternative, bottom up methods to produce monolayer MoS_2 are more promising for large-scale production.

1.3.2 Bottom up methods

Chemical vapor deposition (CVD) is a versatile and sophisticated process for generating coatings and thin films.[46] CVD technology and techniques have been comprehensively developed in many

trades such as in the light emitting diode (LED) industry, for thin metallic and dielectric films in the semiconductor industry, corrosion-resistant films for the aerospace industry, and for coating superhard materials in the petroleum and tool manufacturing industry.[46] CVD is be defined as the deposition of a solid on a heated surface from a chemical reaction in the vapor phase.[46] This procedure involves a vapor-transfer process in which the deposition species are atoms or molecules. The advantage of CVD is that the process creates uniform films with controllable thickness. In addition, a CVD system can be assembled using inexpensive and readily available equipment and precursors. Like all chemical reactions, a CVD reaction depends on two essential principles. First, the reaction must be thermodynamically favorable, which indicates the direction of the reaction and if it proceeds. Second, the reaction is governed by kinetics, which defines both the transport process and rate-control mechanisms.

CVD techniques have been expanded to include two-dimensional materials as well. CVD synthesis of MoS_2 is essential for the creation of uniform large area films ideal for wafer-scale device fabrication. Chemists have been trying to synthesize single-layer MoS_2 since the first 2-D MoS_2 film was reported in 2005.[41] Beginning in 2012, new CVD methods to produce single-layer MoS_2 have been established. An atomically thin Mo film was deposited on a substrate and treated with S vapor.[48] Similarly, MoO_3 was deposited on a substrate followed by annealing including S vapor at a high temperature.[47] Liu *et al.* reported using dip-coating to deposit a $(NH_4)_2MoS_4$ solution on a substrate, followed by annealing under S vapor.[49] In another report, MoO_3 was vaporized to create a MoO_2 template followed by treatment with S vapor.[50] In all of these methods, the MoS_2 films were always polycrystalline with a non-uniform thickness, typically several layers thick. The electric and optoelectronic performances were significantly lower quality than samples prepared by mechanical exfoliation.

The first method to definitively synthesize single-crystal domain and single-layer MoS_2 was developed by Lee *et al.* using MoO_3 and S precursors on a pretreated substrate.[51] The MoS_2 crystals had three points, but were not quite triangular. Instead, the crystals resembled three-pointed stars. The pretreatment method involved spin coating a reduced graphene-oxide (r-GO) solution on the growth substrate to generate a roughness on the surface. It was hypothesized that the r-GO film created a sticky surface, which the MoO_3 and S precursors could adsorb to and chemically react to generate atomically thin MoS_2. The film had a thickness of ~0.7 nm, within the interlayer spacing thickness of MoS_2. The Raman and photoluminescence signature showed a size-dependent optoelectronic shift, consistent with reports of mechanically exfoliated samples. The field effect transistor (FET) had a mobility of 0.7 $cm^2/V \bullet s$, which is several orders of magnitude less than FETs fabricated from exfoliated samples. Although the MoS_2 crystals were not ideal, this approach opened the door for methods and improvements of CVD synthesized MoS_2 and related TMD materials.

In my PhD dissertation, I will first focus on the synthesis of MoS_2 and WS_2 nanosheet, both of which improve the synthesis from the pre-existing and established method. I will also discuss the synthesis of $MoSe_2$ and WSe_2, both of which are alternative and complementary TMD materials to MoS_2 and WS_2. The synthesis of $MoSe_2$ described represents the first reported synthesis of this material and allowed for the identification of $MoSe_2$ as a potential contender to MoS_2 and 2D materials.[52] The synthesis of WSe_2 was reported as the manuscript was being prepared, but is still a novel contribution to the field.[53] Lastly, I will cover research which examines the direct synthesis of lateral and vertical heterojunctions between MoS_2-$MoSe_2$ and WS_2-WSe_2 and their growth mechanism.[54] The research in this dissertation has helped shape the

field of 2D semiconducting films and the methods described lay a platform for future 2D materials synthesis.

1.4 References

(1) Drexler, K. E., *Nanosystems: Molecular Machinery, Manufacturing, and Computation.* **1992**, New York: John Wiley & Sons.

(2) Murray, C. B.; Kagan, C. R.; Bawendi, M. G., *Annu. Rev. Mater. Sci*., **2000**, *30*, 545-610.

(3) Huang, X.; Zhao, Z.; Cao, L.; Chen, Y.; Zhu, E.; Lin, Z.; Li, M.; Yan, A.; Zettl, A.; Wang, M. Y. *et al*., *Science* **2015**, *348*, 1230-1234.

(4) Frens, G., *Nature* **1973**, *241*, 20-22.

(5) Harris, P. J. F., *Nature* **1986**, *323*, 792-794.

(6) Kroto, H. W.; Heath, J. R.; O'Brien, S. C.; Curl, R. F.; Smalley, R. E., *Nature* **1985**, *318*, 162-163.

(7) Duan, X.; Huang, Y.; Cui, Y.; Wang, J.; Lieber, C. M., *Nature* **2001**, *409*, 66-69.

(8) Duan, X.; Lieber, C. M., *Adv. Mater*., **2000**, *12*, 298-302.

(9) Huang, Y.; Duan, X.; Wei, Q.; Lieber, C. M., *Science* **2001**, 291, 630-633.

(10) Benthune, D. S.; Kiang, C. H.; De Vries, M. S.; Gorman, G.; Savory, R.; Vazquez, J.; Beyers, R., *Nature* **1993**, *363*, 605-607.

(11) Iijima, S.; Ichihashi, T., *Nature* **1993**, *363*, 603-605.

(12) West, A. R., *Basic state chemistry*, **1999**, New York: John Wiley & Sons.

(13) Chung, D. D. L., *J. of Mater. Sci.*, **2002**, *37*, 1475-1489.

(14) Fradkin, E., *Phys. Rev. B* **1986**, *33*, 3263-3268.

(15) Novoselov, K. S.; Geim, A. K.; Morozov, S. V.; Jiang, D.; Zhang, Y.; Dubonos, S. V.; Grigorieva, I. V.; Firsov, A. A., *Science* **2004**, *306*, 666-669.

(16) Castro, E. V.; Ochoa, H.; Katsnelson, M. I.; Gorbachev, R. V. Elias, D. C.; Novoselov, K. S.; Geim, A. K., Guinea, F., *Phys. Rev. Lett*. **2010**, *105*, 266601.

(17) Balandin, A. A.; Ghosh, S.; Bao, W.; Calizo, I.; Teweldebrhan, D.; Miao, F.; Lau, C. N., *Nano Lett.* **2008**, *8*, 902.

(18) Stankovich, S.; Dikin, D. A.; Dommett, G. H. B.; Kohlhass, K. M.; Zimney, E. J.; Stach, E. A.; Piner, R. D.; Nguyen, S. T.; Ruoff, R. S., *Nature* **2006**, *442*, 282.

(19) Khrapach, I.; Withers, F.; Bointon, T. H.; Polyushkin, D. K.; Barnes, W. L.; Russo, S.; Craciun, M. F., *Adv. Mater*. **2012**, *24*, 2844.

(20) Weiss, N. O.; Zhou, H.; Liao, L.; Liu, Y.; Jiang, S.; Huang, Y.; Duan, X., *Adv. Mater*. **2012**, *24*, 5782-5825.

(21) Zhou, H.; Yu, W. J.; Liu, L.; Cheng, R.; Chen, Y.; Huang, X.; Yuan, L.; Yang, W.; Huang, Y.; Duan, X., *Nat. Commun*. **2013**, *4*, 2096.

(22) Liao, L.; Lin, Y. C.; Bao, M.; Cheng, R.; Bai, J.; Liu, Y.; Qu, Y.; Wang, K. L.; Huang, Y.; Duan, X., *Nature* **2010**, *467*, 305-308.

(23) Xu, Y.; Lin, Z.; Huang, X.; Wang, Y.; Huang, Y.; Duan, X., *Adv. Mater*. **2013**, *25*, 5779-5784.

(24) El-Kady, M. F.; Strong, V.; Dubin, S.; Kaner, R. B., *Science* **2012**, *335*, 1326-1330.

(25) Chhowalla, M.; Shin, H. S.; Eda, G.; Li, L. J.; Loh, K. P.; Zhang, H., *Nature Chem*. **2013**, *5,* 263-275.

(26) Enyashin, A. N.; Seifert, G., *Nanosystems: Physics, Chemistry, Mathematics*, **2014**, *5*, 517-539.

(27) Sebenik, R. F., *et al*., "Molybdenum and Molybdenum Compounds" in *Ullmann's Encyclopedia of Chemical Technology*. Wiley-VCH, Weinheim. **2005**.

(28) Kobayashi, K.; Yamauchi, J., *Phys. Rev. B*, **1995**, *51*, 17085.

(29) Topsøe, H.; Clausen, B. S.; Massoth, F. E., **1996**, *Hydrotreating Catalysis, Science and Technology*. Berlin: Springer-Verlag.

(30) Liang, T.; Sawyer, W. G.; Perry, S. S.; Sinnott, S. B.; Phillop, S. R., *Phys. Rev. B* **2008**, *77*, 104105.

(31) Kam, K. K.; Parkinson, B. A., *J. Phys. Chem*. **1982**, *86*, 463-467.

(32) Fivaz, R.; Mooser, E.; *Phys. Rev.* **1967**, *163*, 743-755.

(33) Mattheiss, L. F. *Phys. Rev. B* **1973**, *8*, 3719-3740.

(34) Splendiani, A.; Sun, L.; Zhang, Y.; Li, T.; Kim, J.; Chim, C. Y.; Galli, G.; Wang, F., *Nano Lett*. **2010**, *10*, 1271-1275.

(35) Li, T.; Galli, G., *J. Phys. Chem. C* **2007**, *44*, 16192-16196.

(36) Wang, Q. H.; Kalantar-Zadeh, K.; Kis, A.; Coleman, J. N.; Strano, M. S. *Nat. Nanotechnol.* **2012**, *7*, 699–712.

(37) Radisavljevic, B.; Radenovic, A.; Brivio, J.; Giacometti, V.; Kis, A. Single-layer MoS_2 transistors. *Nat. Nanotechnol*. **2011**, *6*, 147-150.

(38) Yin, Z.; Li H.; Li, H.; Jiang, L.; Shi, Y.; Sun, Y.; Lu, G.; Zhang, Q.; Chen, X.; Zhang, H., *ACS Nano* **2012**, *6*, 74-80.

(39) Li, D.; Cheng, R.; Zhou, H.; Wang, C.; Yin, A.; Chen, Y.; Weiss, N. O.; Huang, Y.; Duan, X., *Nat. Commun*. **2015**, *6*, 7509.

(40) Jiang. S.; Cheng, R.; Ng, R.; Huang, Y.; Duan, X., *Nano Res*. **2015**, *8*, 257-262.

(41) Novoselov, K. S.; Jiang, D.; Schedin, F.; Booth, T. J.; Khotkevich, V. V.; Morozov, S. V.; Geim, A. K., *Proc. Nath. Acad. Sci*., **2005**, *102*, 10451-10453.

(42) Coleman, N. J.; Lotya, M.; Nicolosi, V., *et al*. **Science** *2011*, 311, 568.

(43) Zeng, Z.; Yin, Z.; Huang, X.; Li, H.; He, Q.; Lu, G.; Boey, F.; Zhang, H., *Angew. Chem. Int. Ed.* **2011**, *50*, 11093-11097.

(44) Gomez-Castellanos, A.; Barkelid, M.; Gossens, A. M.; Calado, V. E.; van der Zant, H. S. J.; Steele, G. A., *Nano Lett.* **2012**, *12*, 3187-3192.

(45) Liu, Y.; Nan, H.; Wu, X.; Pan, W.; Wang, W.; Bai, J.; Zhao, W.; Sun, L.; Wang, X.; Ni, Z., *ACS Nano*, **2013**, *7*, 4202-4209.

(46) Pierson, H. O., *Handbook of Chemical Vapor Deposition (CVD)*, **1999**, Park Ridge, New Jersey: Noyes Publications.

(47) Lin, Y. C.; Zhang, W.; Huang, J. K.; Liu, K. K.; Lee, Y. H.; Liang, C. T.; Chu, C. W.; Li, L. J., *Nanoscale* **2012**, *4*, 6647-6641.

(48) Zhan, Y.; Liu, Z.; Najmaei, S.; Ajayan, P. M.; Lou, J., *Small* **2012**, *8*, 966-971.

(49) Liu, K. K.; Zhang, W. J.; Lee, Y. H.; Lin, Y. C.; Chang, M. T.; Su, C. Y.; Chang, C. S.; Li, H.; Shi, Y. M.; Zhang, H. *et al. Nano Lett.* **2012**, *12*, 1538-1544.

(50) Wang, X.; Feng, H.; Wu, Y.; Jiao, L.; *J. Am. Chem. Soc*. **2013**, *135*, 5304-5307.

(51) Lee, Y. H.; Zhang, X. Q.; Zhang, W. J.; Chang, T. M.; Lin, C. T.; Chang, K. D.; Yu, Y. C.; Wang, J. T. W.; Chang, C. S.; *et al. Adv. Mater*. **2012**, *24*, 2320-2325.

(52) Shaw, J. C.; Zhou, H.; Chen, Y.; Weiss, N. O.; Liu, Y.; Huang, Y.; Duan, X., *Nano Res*. **2014**, *7*, 511-517.

(53) Zhou, H.; Wang, C.; Shaw, J. C.; Cheng, R.; Chen, Y.; Huang, X.; Liu, Y.; Weiss, N. O.; Lin, Z.; Huang, Y.; Duan, X., *Nano Lett*. **2014**, *15*, 709-713.

(54) Duan, X.; Wang, C.; Shaw, J. C.; Cheng, R.; Chen, Y.; Lai, H.; Wu, X.; Tang, Y.; Zhang, Q.; Pan, A.; *et al. Nat. Nanotechnol*. **2014**, *9*, 1024-1030.

(55) Geim, A. K.; Novoselov, K. S., *Nat. Mater*. **2007**, *6*, 183-191.

Chapter 2. The synthesis of MoS_2

2.1 Introduction

As mentioned in the introduction, several attempts were made to isolate a 2-D MoS_2 sheet from its bulk counterpart. Methods included liquid exfoliation, direct sulfination of dip-coated $(NH_4)_2MoS_4$, and thermally evaporated Mo or MoO_3.[1-4] The isolated MoS_2 crystals were thin, but none were conclusively an isolated a single layer of MoS_2. The first undeniable synthesis of monolayer MoS_2 was reported in 2012 by Lee *et al*. using a chemical vapor deposition (CVD) method.[5] The group used a substrate coated with sub-micron scale reduced graphene oxide (r-GO) flakes to create a sticky surface. Next, they co-evaporated S and MoO_3 powders in a horizontal tube furnace. The synthesized MoS_2 was triangular with sharp, star-shaped edges but of lower crystalline quality, as evident by less-intense Raman and PL emission. In this chapter, a refined and improved method of growing single layer MoS_2 is described. High quality MoS_2 was grown using MoO_3 and S powders on an untreated substrate, and featured distinctive triangular edges with edge lengths up to 100 μm.

2.2 Methods

The reaction occurred in a horizontal tube furnace (Lindberg Blue M) in a 1-inch diameter quartz tube (Fig. 2.1). 0.2 g of MoO_3 was placed inside a 5-mL alumina boat in the center of the furnace, two cm upstream of the built-in thermocouple. Several pieces of untreated 300 nm SiO_2/Si were place on top of the boat containing MoO_3, with their polished side facing the powder. The pieces were approximately 2 cm x 2 cm. At the upstream end of the tube furnace, 0.5 g of S powder was placed in a 5-mL alumina boat, which was slightly outside of the heading zone by approximately 5 cm. The downstream end of the tube was attached to a quick (KF) connection, which was attached to ¼ inch inner diameter, 5-foot long plastic PTFE that led

directly to an exhaust bank. Before the reaction, the furnace was purged with argon (Ar) for one hour at 100 standard cubic centimeters per minute (sccm). The furnace was then activated and heated to 750 °C at a ramp rate of 50 °C/min. When the furnace reached 725 °C, the quartz tube was manually moved 5 cm downstream. The tube was shifted such that the S powder entered at an area in the furnace where the temperature was maintained at ~100 °C, as to be sufficiently vaporized over the course of the reaction. After 10 minutes, the S powder was completely vaporized and the cold downstream end of the tube became thoroughly coated in solid sulfur. After 10 minutes, the furnace was deactivated and cooled slowly to room temperature. When the furnace reached room temperature, the quartz tube was opened and the nanosheets were characterized.

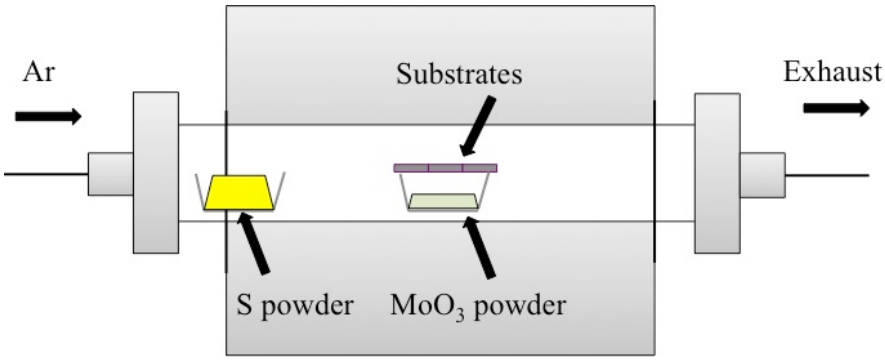

Figure 2.1. MoO_3 powder and elemental S powders were used as the solid source. MoO_3 was placed inside a 5-ml alumina boat at the center of the furnace. The 300 nm SiO_2/Si substrates were placed polished side down on the MoO_3 boat. S powder was placed in an alumina boat upstream in the quartz tube, and was shifted into the heating zone at the reaction temperature.

2.3 Results and Discussion

After the reaction, the polished side of the furnace had a bluish shade, which covered areas up to several hundred microns. Upon closer inspection using optical microscopy (OM), 10x magnification revealed the blue film was nearly dispersed uniformly across the edges of the substrate (Fig. 2.2 a). Higher magnifications of 50x and 100x (Fig. 2.2 b, c) revealed the blue

film essentially comprises of randomly orientated triangular crystals. The triangular MoS_2 nanosheets grew indiscriminately and with no particular alignment on the substrate, indicating the growth was non-epitaxial (Fig 2.2 c, d). Clusters of MoS_2 nanosheets nucleated and grew into triangular domains, which merged together to form small-area films (Fig 2.2 e). The films were uniform in contrast and composition, indicating a homogeneity and monodispersity within the size and shape of the nanosheets. The MoS_2 nanosheets are stable in air up to several weeks, as no obvious degradation was observed. An optical contrast exists between thick and thin MoS_2 crystals, which distinguish the number of layers. At 100x magnification, thick MoS_2 appears darker blue or yellow while monolayer and bilayers appear purple and dark purple, respectively (Fig. 2.2 f).

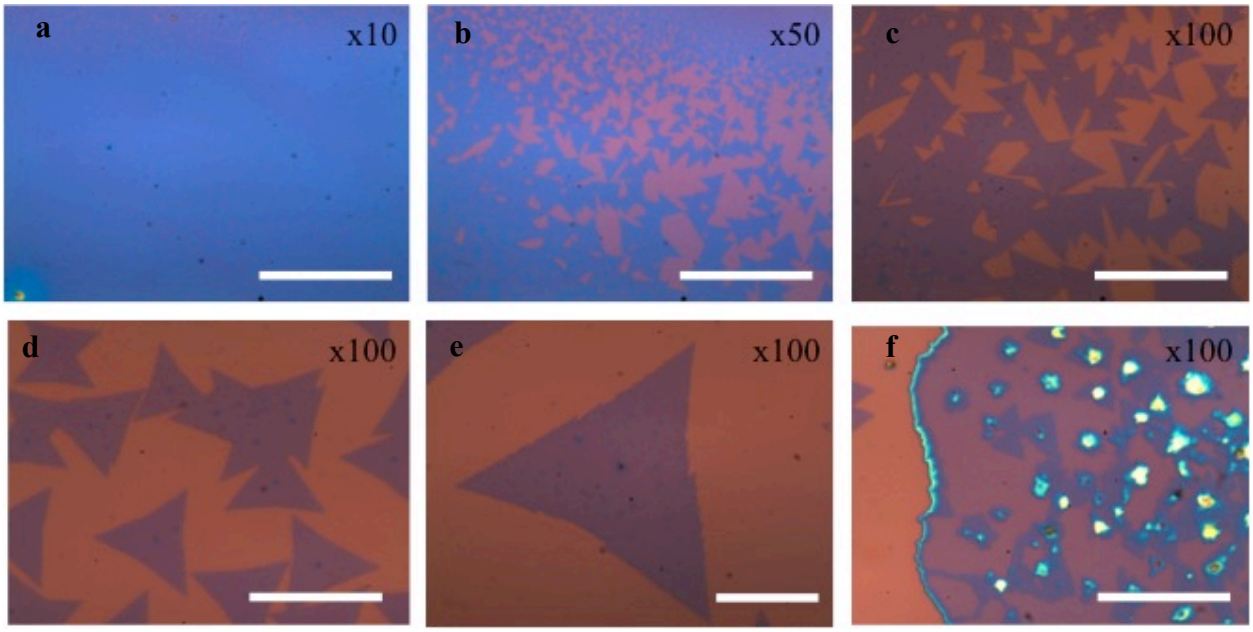

Figure 2.2. (a) 10x magnification optical micrograph of MoS_2 single layer domains covering the substrate. Scale bar is 200 µm. **(b)** 50x enhances optical micrograph of (a). Scale bar is 100 µm. **(c)** 100 x magnification optical micrograph of (b). The triangular MoS_2 nanosheets are all uniform in composition and shape. Some nanosheets merge to form films lesser area films. Scale bar is 50 µm. **(d)** MoS_2 triangular domains clustered on the substrate. Some of the domains merged together to form films. **(e)** Large area MoS_2 monolayer. **(f)** Film showing a MoS_2 underlying film with clusters of bilayer (darker purple) and thick multilayer (blue and yellow) crystals. Scale bars for (d-f) are 25 µm.

Using MoO_3 and S precursors to synthesize MoS_2 fullerenes has been previously described and can be used to describe the reaction to grow of the MoS_2 nanosheets.[6]

$$7\ S + 2\ MoO_3 \rightarrow 2\ MoS_2 + 3\ SO_2$$

The chemical reaction may be an over simplification of the actual reaction process. Even in the absence of a reducing agent (H_2 or S), MoO_3 decomposes to MoO_2 when heated, similar to other reports.[7] The rhomboidal MoO_2 byproducts sheets are also flat and atomically thin, and are primarily located at the center of the growth substrate, directly under the MoO_3 powder (Fig. 2.3). By comparison, the MoS_2 nanosheets are located towards the edges of the substrate and at the interface where the substrate meets the boat. The MoO_2 byproducts and the MoS_2 nanosheets are segregated, as no MoS_2 crystals were observed to grow on the MoO_2.

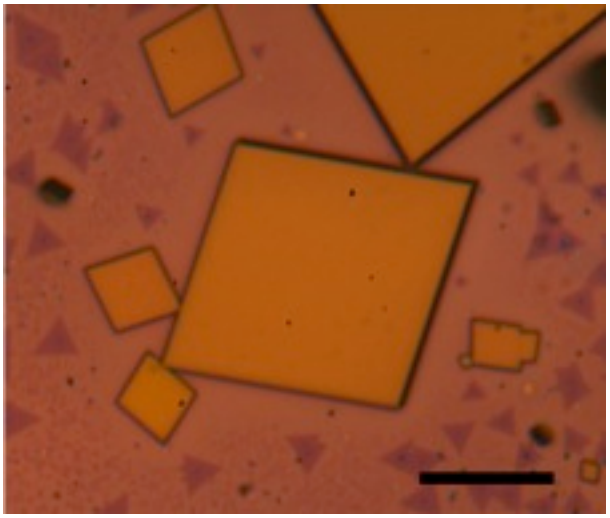

Figure 2.3. MoO_2 crystal (orange rhomboidal crystal) byproduct from the chemical reaction to synthesize MoS_2. The MoS_2 is located near the MoO_2 but doesn't grow on the MoO_2 itself (smaller triangular crystals). Scale bar is 10 μm.

Scanning electron microscopy (SEM) demonstrates that the triangular MoS_2 crystals are distinguishable from the growth substrate. The MoS_2 nanosheets are uniform, with no obvious holes or defects on the surface (Fig. 2.4 a). There is a varying, irregular shaded region within the MoS_2 film located at the center of the crystal that represents bilayer MoS_2 (Fig. 2.4 b). It is possible the center/nucleation region has more defects or protrusions, and is therefore more susceptible to additional layer nucleation and growth. Atomic force microscopy (AFM) was used to verify the thickness and uniformity of the MoS_2 nanosheet (Fig. 2.4 c). An AFM scan of the MoS_2 nanosheet shows the height difference between the substrate and the crystal edge to be ~ 0.65 nm, which corresponds to the interlayer spacing of MoS_2 (Fig. 2.4 d). There are some protrusions across the nanosheet, indicating the film is not atomically flat. The lumps could be due to defects or grains across the nanosheet, at which excess precursors congregates and grow into small 3-D structures.

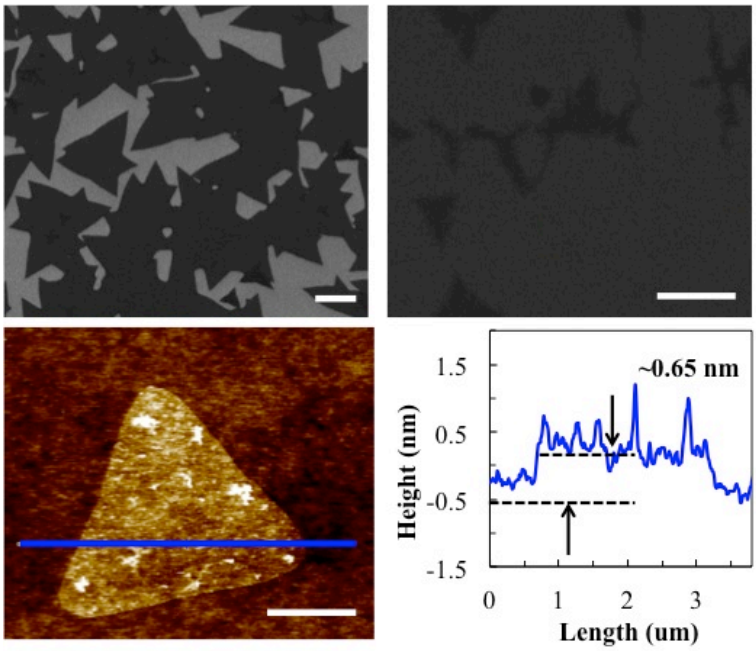

Figure 2.4 (a) Scanning electron micrograph (SEM) of MoS_2 monolayer crystals on the growth substrate. Some nanosheets have merged together forming small films. Scale bar is 10 µm. **(b)** SEM image showing a single layer with bilayer (darker contrast) triangles and irregular shapes. The longer, river like bilayers likely follow grains formed when the monolayers merged together. Scale bar is 5 µm. **(c)** Atomic force micrograph of a monolayer MoS_2 crystal. Scale bar is 1 µm. **(d)** Height scan of (c) at the blue line showing the crystal is monolayer with a thickness of ~ 0.65 nm.

Raman spectroscopy can be utilized to both verify the crystal structure and probe the size-dependent vibrational properties. Raman spectrum measurements were taken using a Horiba spectrometer with a continuous 514 nm, 50-μW laser. The Raman spectrum was taken on both a thick and thin MoS_2 crystal (Fig. 2.5). For MoS_2, there are two notable Raman shifts that identify the crystal; the out-of-plane A_{1g} and the in-plane E_{2g}. The Raman spectra for the thick (bulk) MoS_2 crystal shows the A_{1g} and E_{2g} peaks located at 407.3 cm^{-1} and 381.0 cm^{-1} respectively, which closely matches values reported in literature.[9] On the other hand, single layer MoS_2 has Raman values which shift from the bulk counterpart. The peaks for A_{1g} and E_{2g} are located at 403.3 cm^{-1} and 383.0 cm^{-1}, respectively. These changes are in agreement with other reports on monolayer MoS_2.[9]

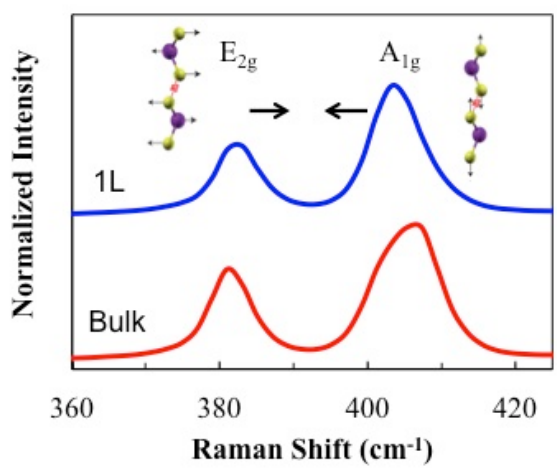

Figure 2.5. Raman spectrum of single-layer (blue line) and bulk (red line) MoS_2 nanosheets. The Monolayer MoS_2 has E_{2g} and A_{1g} modes at 383.0 cm^{-1} and 403.3 cm^{-1} respectively. Bulk MoS_2 has E_{2g} and A_{1g} modes at 407.3 cm^{-1} and 381.0 cm^{-1} respectively.

Photoluminescence (PL) emission measurement was used to investigate the direct band gap of monolayer MoS_2. PL was measured using a Horiba spectrometer with a 514 nm, 50-μW continuous laser for one second (Fig. 2.6). When monolayer MoS_2 (blue line) was excited with

the laser, intense emission was observed at 670 nm (1.85 eV), identifying the optical direct band gap. The thicker bulk MoS_2 (red line) had a significantly relaxed emission compared to the monolayer region, but a small bump was observed, which peaked at 670 nm. The emission was 50x less intense than the monolayer. The intensity of the laser was enough to excite enough some electrons at the direct band gap region (K➔K) of the electronic structure, but at a significantly lower yield than the monolayer.

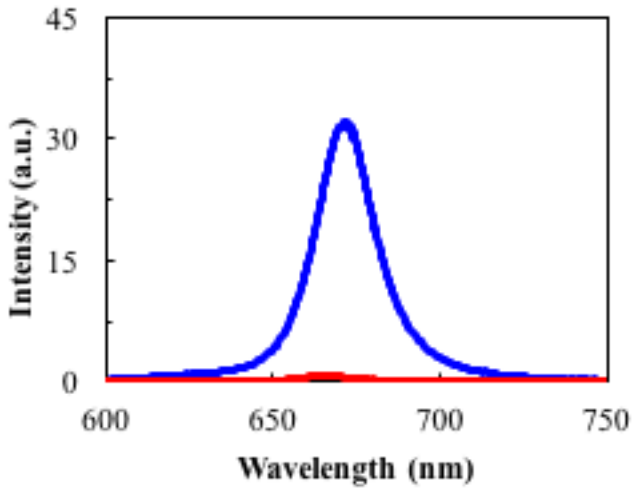

Figure 2.6. Photoluminescence spectra of mono and bilayer MoS_2. Monolayer MoS_2 (blue line) has intense emission at 670 nm, matching the optical band gap. Thicker, bulk MoS_2 (red line) has 50x less intense emission, but has a small bump at 670 nm, indicating with enough laser power, some direct band gap emission (K➔K) is observed.

2.4 Conclusion

MoS_2 single and few-layer triangular nanosheets were grown directly onto 300 nm SiO_2/Si substrates. The MoS_2 nanosheets were optically distinguishable and had edge lengths up to 100 µm. Atomic force microscopy confirmed the thickness of a single layer was ~ 0.65 nm. Raman spectroscopy established that MoS_2 vibrational modes shift from the A_{1g} 407.3 cm^{-1} and E_{2g} 381.0 cm^{-1} in bulk, to A_{1g} 403.3 cm^{-1} and E_{2g} 383.0 cm^{-1} as a single layer. Photoluminescence emission of MoS_2 single layers had an intense peak at 670 nm,

corresponding to the 1.9 eV optical direct band gap. Thicker MoS_2 has had significantly reduced emission since the primary electronic pathway is a lower energy indirect band gap.

2.5 References

(1) Coleman, J. N.; Lotya, M.; Nicolosi, V. *et al., Science*, **2011**, *331*, 568.

(2) Liu, K. K.; Zhang, W. J.; Lee, Y. H.; Lin, Y. C.; Chang, M. T.; Su, C. Y.; Chang, C. S.; Li, H.; Shi, Y. M.; Zhang, H.; Lai, C. S.; Li, L. J., *Nano Lett.,* **2012**, *12*, 1538-1544.

(3) Zhan, Y.; Liu, Z.; Najmaei, S.; Ajayan, P. M.; Lou, J, *Small* **2012**, *8*, 966-971.

(4) Lin, Y. C.; Zhang, W. J.; Huang, J. K.; Liu, K. K.; Lee, Y. H.; Liang, C. T.; Chu, C. W.; Li, L. J. Nanoscale, **2012**, *4*, 6637.

(5) Lee, Y. H.; Zhang, X. Q.; Zhang, W. J; Chang, T. M.; Lin, C. T.; Chang, K. D.; Yu, Y. C.; Wang, J. T. W.; Chang, C. S.; Li, L. J.; Lin, Y. W., *Adv. Mater*., **2012**, *24*, 2320-2325.

(6) Li, X. L.; Li, Y. D., *Chem. Eur. J*., **2003**, *9*, 2726-2731.

(7) Wang, X.; Feng, H.; Wu, Y.; Jiao, L., *JACS*, **2013**, *135*, 5304-5307.

(8) Jellinek, F.; Brauer, G.; Muller, H., *Nature*, **1960**, *185*, 376-377

(9) Lee, C.; Yan, H.; Brus, L. E.; Heinz, T. F.; Hone, J.; Ryu, S. *ACS Nano*, **2010**, *4*, 2695-2700.

(10) Spelndani, A.; Sun, L.; Zhang, Y.; Li, T; Kim, J.; Chim, C. Y.; Galli, G.; Wang, F., *Nano. Lett*. **2010**, *10*, 1271-1275.

Chapter 3. The synthesis of WS_2

3.1 WS_2 synthesis

WS_2 is closely related both physically and structurally and to MoS_2, with W atoms replacing the Mo atoms.[1] WS_2 can be isolated into atomically thin nanosheets, that have an indirect-to-direct band gap transition (1.4 eV to 2.1 eV) as the material is thinned to a single layer.[2] Similarly to MoS_2, WS_2 is an attractive material for optoelectronic devices such as photodetectors and field effect transistors.[2,7] When we started researching WS_2 synthesis, WS_2 monolayer synthesis and growth was unreported in literature. We developed a chemical vapor deposition (CVD) approach using WO_3 and S powders to synthesize and grow WS_2 nanosheets. The WS_2 nanosheets were ~ 1 nm thick based on atomic force microscopy height scans. The Raman response showed a clear shift in peak position in monolayer and bulk WS_2 crystals. Additionally, WS_2 and had intense photoluminescence emission at 640 nm (1.94 eV), corresponding to the direct band gap.

3.2 Methods

The reaction occurred in a 12-inch horizontal tube furnace (Lindberg Blue M) in a 1-inch diameter quartz tube (Fig. 3.1). 0.02g of WO_3 powder (Sigma Aldrich, 99.5% purity) was sprinkled on top of three ~ 2 × 2 cm 300 nm SiO_2/Si wafers placed at the center of the furnace. 0.2g of S powder (Sigma Aldrich, 99.5%) was placed in a 5 mL alumina boat upstream to the edge of the furnace, outside of the heating zone. The tube was evacuated and purged several times in 100 standard cubic centimeters per minute (sccm) of Ar carrier gas for one hour. For the reaction, the flow was reduced to 50 sccm Ar. The furnace was heated 50 °C/min to the growth temperature of 850 °C under atmospheric pressure. When the furnace reached 825 °C, the tube was physically moved so the S was located heated edge of the furnace in order to

sufficiently vaporize over the course of the reaction. The furnace was kept at 850 °C for ten to twenty minutes, after which it was cooled down to room temperature.

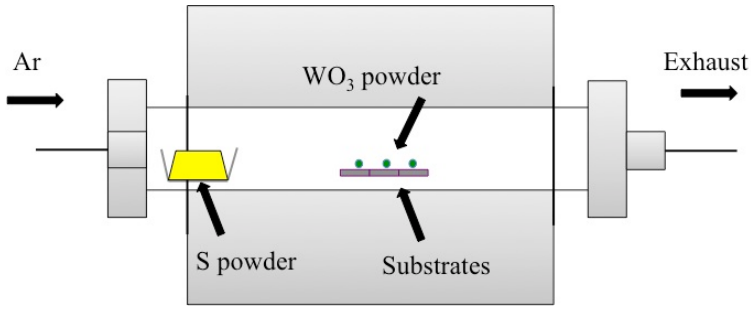

Figure 3.1. WO_3 powder and elemental S powders were used as the solid source. WO_3 powder was sprinkled over the substrates in the hot center zone of the furnace. The S vapor was sequentially introduced into the CVD reaction by shifting quartz tube rightward to move the S source into the furnace without breaking vacuum.

3.3 Results and Discussion

The WS_2 nanosheets grew into distinguishable single and few-layer domains clustered randomly on the substrate, as shown by optical microscopy (OM) (Fig. 3.2a). The WS_2 nanosheets consisted primarily of triangular single-crystal domains with edge lengths typically between 5 μm and 30 μm (Fig. 3.2b), comparable to MoS_2. There were fewer nanosheets on the substrate compared to MoS_2 synthesis, which can be attributed to the lower volatility of WO_3

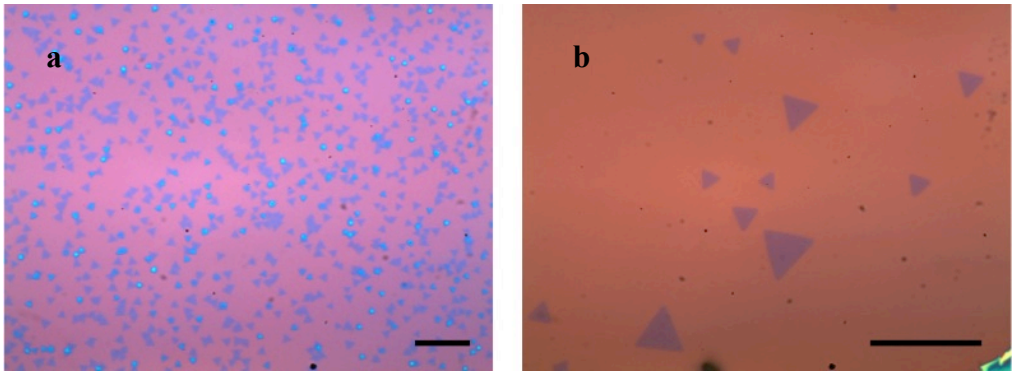

Figure 3.2 (a) Single and few-layer WS_2 domains clustered on a 300 nm SiO_2/Si substrate at 10x magnification. Scale bar is 100 μm. **(b)** Enhanced image of several WS_2 monolayers at 100x magnification.

compared to MoO_3. The driving force behind the triangular growth is based on the WS_2 trigonal prismatic crystal structure, with the thermodynamically favorable S terminated edges.[1] The single-domain crystal grew into the triangular crystal by repeating its unit cell.

Atomic force microscopy (AFM) was used to characterize a WS_2 domain (Fig. 3.3 a). The AFM image reveals the WS_2 crystal to is a triangular monolayer with a triangular edge length of ~6 μm. The AFM image revels an atomically smooth basal plane of the nanosheet, with no significant dips or abrasions protruding from the basal plane. The height profile of a WS_2 nanosheet grown directly on the substrate has a thickness of ~1 nm, closely matching the interlayer spacing of WS_2 and previously reported WS_2 monolayer exfoliations (Fig. 3.3 b).[1,2]

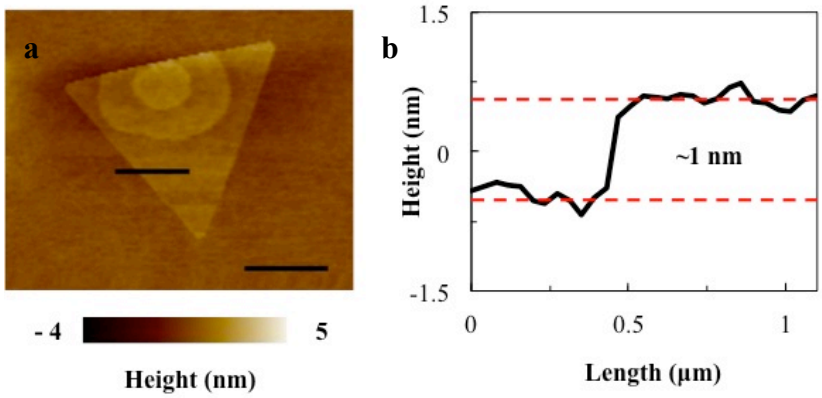

Figure 3.3 (a) Atomic force micrograph of a WS_2 crystal. The line scan (black line across the crystal) is across a monolayer region, but bilayer and trilayer WS_2 planes are present. The scale bar is 2 μm. **(b)** Line scan from (a) showing the thickness of the WS_2 monolayer is 1 nm.

Raman spectroscopy is a valuable method to probe the acoustic vibrations and crystal signature of single and few-layer WS_2. The Raman spectrum of single and few-layer WS_2 crystals were measured using a Horiba spectrometer with a continuous 514 nm, 50 μW laser (Fig. 3.4). WS_2 has two prominent and identifying modes; the out-of-plane A_{1g} and the in-plane E_{2g}.[8] The A_{1g} vibrational mode occurs when the two S atoms oscillate out of the plane of the WS_2 layer with the W atom remaining stagnant. The reported bulk A_{1g} peak is located at 421 cm^{-}

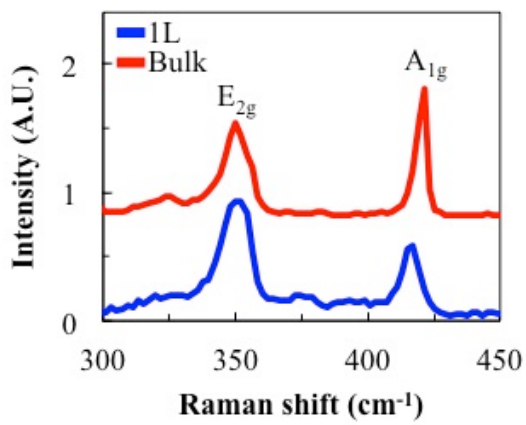

Figure 3.4 Raman spectrum of WS_2 monolayer (blue line) and bulk (red line) A_{1g} and E_{2g} modes. The WS_2 monolayer A_{1g} is 417 cm^{-1} and E_{2g} is 352 cm^{-1}. The bulk WS_2 421 A_{1g} is cm-1 and E_{2g} is 350 cm^{-1}.

[1,8] The E_{2g} vibrational mode occurs when the S and W atoms oscillate within the plane of the WS_2 layer. The reported bulk E_{2g} peak is located at 350 cm^{-1}.[8] When WS_2 is thinned to a single-layer, the vibrational modes shift. The A_{1g} mode relaxes to 417 cm^{-1} as a monolayer nanosheet.[13] The E_{2g} stiffens to 352 cm^{-1} as a monolayer.

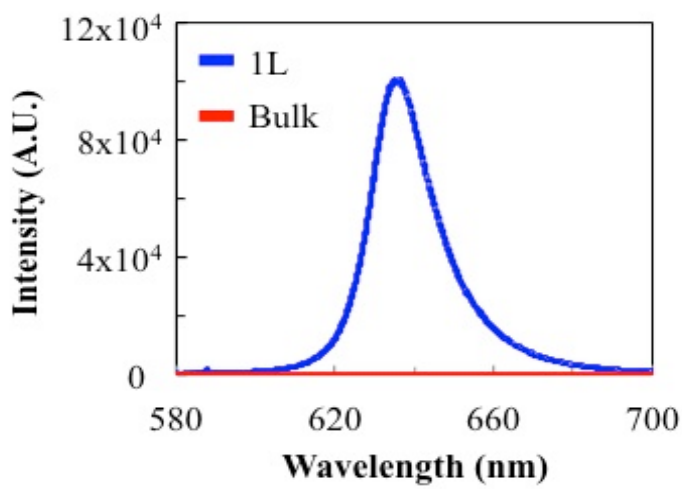

Figure 3.5 Photoluminescence emission spectrum of monolayer (blue line) and bulk (red line) WS_2 domains. Monolayer photoluminescence emission peak is centered at 640 nm (1.94 eV).

WS_2 monolayer and multilayer photoluminescence (PL) emission was measured using a Horiba Raman spectrometer with a 514 nm, 50 μW continuous laser, activated for 1 s (Fig. 3.5). The PL emission for multilayered WS_2 showed no noticeable peak across the visible spectrum. However, PL emission for monolayer WS_2 had strong emission centered at 640 nm (1.94 eV). The emission peak is broad with a full width half maximum value of 28 nm (0.07 eV). The fact that emission is only observed when WS_2 is thinned to a monolayer is significant because only two-

dimensional WS_2 has a direct band gap.[2] The emission of bilayer and multilayer WS_2 remains in the lower-energy indirect band gap counterpart.

3.4 Conclusion

In summary, monolayer, bilayer and few layer WS_2 has been synthesized by CVD by vaporizing WO_3 and S powders in a tube furnace. The crystals were first observed by optical microscopy and the thickness-dependent optical contrast was identified. The atomic levelness of the WS_2 crystal planes and their 1 nm layer thickness was confirmed by atomic force microscopy. Raman spectroscopy verified the crystal structure, and also showed a thickness-dependent phonon shift of the out-of-plane A_{1g} and in-plane E_{2g} vibrational modes The shift occurred from 421 cm^{-1} to 417 cm^{-1} for the A_{1g} mode, and 350 cm^{-1} to 352 cm^{-1} for the E_{2g} mode. Photoluminescence emission discovered the 640 nm direct band gap emission of monolayer WS_2. Thicker WS_2 had no observable emission in the visible spectrum, confirming photoluminescence emission only occurs on monolayer WS_2 crystals.

3.5 References

(1) Wilson, J. A.; Yoffe, A. D., *Adv. Phys*. **1969**, *18*, 193–335.

(2) Zhao, W.; Ghorannevis, Z.; Chu, L.; Tohi, M.; Kloc, C.; Tan, P. H.; Eda, G., *ACS Nano,* **2013**, *7*, 791-797.

(3) Braga, D.; Gutiérrez Lezama, I.; Berger, H.; Morpurgo, A. F., *Nano Lett*. **2012**, *12*, 5218–5223.

(4) Fang, H.; Chuang, S.; Chang, T. C.; Takei, K.; Takahashi, T.; Javey, A. *Nano Lett.* **2012**, *12*, 3788–3792.

(5) Kuc, A.; Zibouche, N.; Heine, T. *Phys. Rev*. B **2011**, *83*, 245213.

(6) Yun, W. S.; Han, S. W.; Hong, S. C.; Kim, I. G.; Lee, J. D. *Phys. Rev. B* **2012**,

85,033305.

(7) Jiang, H., *J. Phys. Chem. C,* **2012**, *116*, 7664–7671.

(8) Molina-Sanchez, A.; Wirtz, L. *Phys. Rev. B*, **2011**, *84*, 155413.

Chapter 4. The synthesis of $MoSe_2$

4.1 Introduction

$MoSe_2$ is another member of the transition metal dichalcogenide family similar to MoS_2, except with Se replacing the S atoms. Like other transition metal dichalcogenides, MoSe2 is attractive in numerous industrial and academic research fields such as catalysis, energy storage, dry lubrication, microelectronics and optoelectronics.[1-7] Recently, significant research has focused on the isolation of 2D TMDs due to their unique transformation from an indirect to a direct band gap when confined to a single layer.[8-10] In regards to $MoSe_2$, 3-D $MoSe_2$ has an indirect band gap of 1.1 eV, while 2D $MoSe_2$ has a direct band gap of 1.5 eV.[32,33] These atomically thin nanosheets are of particular interest for new types of electronic/optoelectronic devices and chemical sensors.[11-18]

While there have been numerous reports on synthesis of single and few-layer nanosheets of the sulfide family of dichalcogenides (MoS_2 and WS_2),[19-24] the synthesis and characterization of the selenide family ($MoSe_2$ and WSe_2) remains largely unexplored.[25] Several bottom-up syntheses of thin films and clusters of $MoSe_2$ have been reported,[26-31] yet most studies of single layers are based on top-down, mechanically-exfoliated monolayers using Scotch tape.[32,33] Combining these nanosheets into heterostructures of TMDs have been explored theoretically, and can lead to intriguing structures designed with specifically engineered properties.[34] For $MoSe_2$ to be implemented in electronic devices and hetero-integrated nanostructures, controllable synthesis of large-area, single- and few-layered crystals is a necessity.

To this end, chemical vapor deposition (CVD) represents an attractive approach for the growth of $MoSe_2$ nanosheets on a supporting substrate, exploiting the anisotropic bonding characteristics of layered materials used to synthesize a number of other 2D materials including

MoS_2 and WS_2.[19-24,35,36,42] Here we report the first synthesis of $MoSe_2$ monolayers using a CVD approach by using solid Se and MoO_3 powders in a reducing atmosphere under ambient pressures, depositing directly on untreated 300 nm SiO_2/Si substrates (Fig. 4.1).

4.2 Methods

The reaction took place in a 12-inch horizontal tube furnace (Lindberg Blue M) in a 1-inch diameter quartz tube (Fig. 4.1). 0.25g of MoO_3 powder (Sigma Aldrich, 99.5% purity) was placed in a 5 mL alumina boat at the center of the furnace with ~ 2 × 2 cm 300nm SiO_2/Si wafers placed polished side down on top of the boat. There were ideally 3-4 pieces of SiO_2/Si placed on the boat at the center of the furnace. 0.5g of Se powder (Sigma Aldrich, 99.5%) was placed in a 5 mL alumina boat upstream to the edge of the furnace. The tube was evacuated and purged several times in 100 sccm Ar and 100 sccm H_2 gas for one hour, after which it was brought to ambient pressure. The flow was reduced to 65 sccm Ar and 5 sccm H_2 for one hour. After one hour, the furnace was heated 25 °C/min to the growth temperature of 750 °C. When the furnace reached 700 °C, the tube was manually moved so the Se was at the heated edge of the furnace, just above 300 °C so the Se was adequately heated and vaporized over the course of the reaction. The furnace was kept at 750 °C for ten to fifteen minutes, after which it was cooled down to room temperature. We found highly crystalline $MoSe_2$ triangular domains were deposited on the substrates and had edge lengths up to ~30 μm.

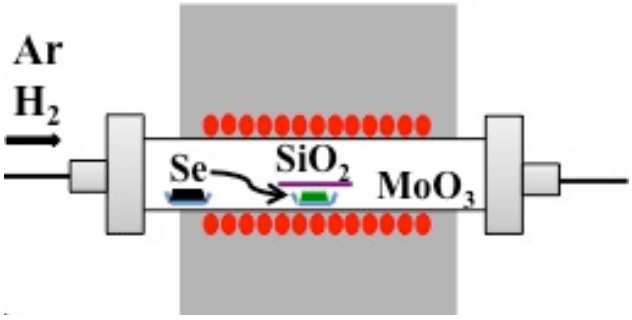

Figure 4.1 Schematic illustrating the basic design of the CVD chamber and furnace. A 1-inch diameter tube displays the relative locations of the solid Se and MoO_3 powders and the 300 nm SiO_2/Si substrate. The red circles represent heating filaments of the furnace.

4.3 Results and Discussion

It is important to emphasize the role that H_2 plays within the reaction. Without the addition of H_2, $MoSe_2$ nanosheets were not observed on the SiO_2/Si substrate. A trace amount of H_2 (5 sccm) is sufficient for $MoSe_2$ crystals to nucleate and grow into extended 2D structures. A recent report on the synthesis of WS_2 and WSe_2 demonstrates the role that H_2 has in the formation of highly crystalline 2D nanosheets.[41,42] We propose that the H_2 reduces the MoO_3 to MoO_{3-x}, which is further reduced by the vaporous Se in a mechanism similar to that of H_2 with S to synthesize MoS_2 fullerenes.[44] The reaction product $MoSe_2$ would then transition from vapor to solid and grow on the substrate. According to this mechanism, the overall reaction is we propose:

$$MoO_3 + H_2 + 3\ Se \rightarrow MoSe_2 + SeO_2 + H_2O$$

The as grown $MoSe_2$ nanosheets and domains were first observed using optical microscopy (OM) (Fig. 4.2 a, c, d), with a thickness dependent contrast that can distinguish between single- and multi-layers on 300 nm SiO_2/Si (Fig. 4.2 c, d). $MoSe_2$ nanosheets were found to have nucleated randomly on the substrate with no specific orientation, and with domains up to several tens of micrometers. Under proper conditions, the domains can merge

together to form continuous thin films up to several hundred microns across (data not shown). Single layers are the most frequently observed (Fig. 4.2 c), but bilayer, trilayer and thicker crystals are seen as well. A scanning electron micrograph (SEM) presents a cluster of monolayer $MoSe_2$ nanosheets (Fig. 4.2 b). Atomic force microscopy (AFM) was used to characterize the $MoSe_2$ nanosheet thickness (Fig. 4.2 e, f). The height of the $MoSe_2$ monolayer on the SiO_2/Si substrate was typically measured between 0.70–1.0 nm, comparable with previous reports of exfoliated $MoSe_2$.[32,37] The second layer height in bilayers is consistently found to be between 0.60-0.70 nm, which is in agreement with the step height difference of 0.65 nm between monolayer and bilayer $MoSe_2$.[40]

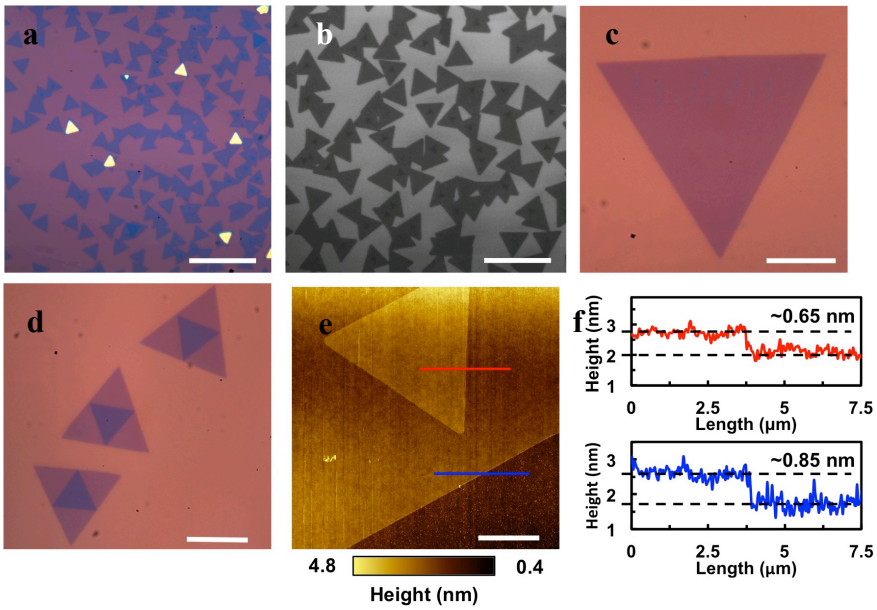

Figure 4.2 (a) Optical micrograph (OM) and **(b)** Scanning electron micrograph (SEM) of a cluster of $MoSe_2$ triangular nanosheet domains. **(c)** OM of a triangular monolayer with an edge length of 50 μm. **(d)** Three monolayer/bilayer crystals with antiparallel triangular bilayers. **(e)** AFM height profile of monolayer/bilayer domains and **(f)** corresponding line scan.

Triangular monolayers were always observed on the substrate, which is consistent with previous reports.[19-24,41,42] This triangular crystal shape is dictated by the thermodynamically favorable edge termination of either Mo or Se atoms and the three-fold symmetry of the half unit

cell of single layer dichalcogenides, compared to the six-fold symmetry of bulk $MoSe_2$.[43,45] Bilayer triangles begin to grow from the same nucleation site at the center of the triangle, but in an antiparallel orientation due to inverted stacking order of AA'.[46] This here-so-called monolayer/bilayer "triforce" structures (Fig. 4.2 d) are predominantly observed, with subsequent layers alternating triangle direction; however, some parallel bilayer triangles are also seen, which may indicated a less favorable AB stacking order.

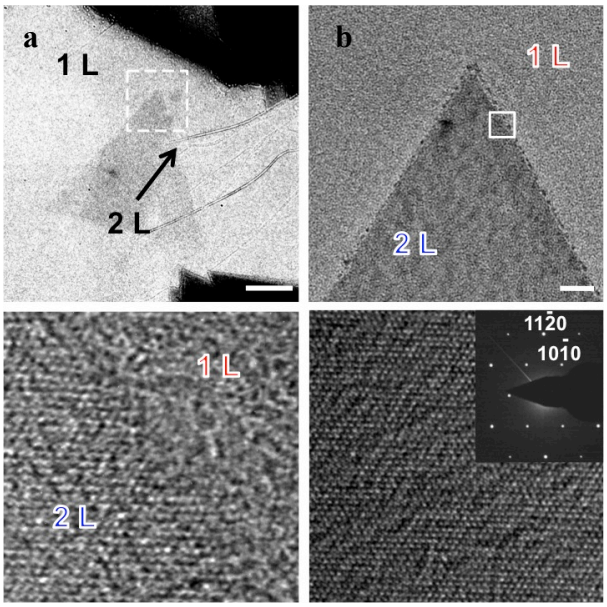

Figure 4.3 (a) Low magnification transmission electron micrograph (TEM) of $MoSe_2$ mono/bilayer (scale bar 2 μm). **(b)** Magnified view of the mono/bilayer interface (scale bar 200 nm). **(c)** TEM image of the marked surface of (b). **(d)** High resolution TEM image of multilayer $MoSe_2$ nanosheet with its corresponding selected area electron diffraction pattern (inset).

The crystal structure of mono-, bi-, and multi-layers was analyzed using high-resolution transmission electron microscopy (HRTEM) (Fig. 4.3 a-d). Figures 4.3a-c show the interface between the mono/bilayer at increasing magnification. The selected area electron diffraction (SAED) confirms the hexagonal $MoSe_2$ structure, which is consistent with the high-resolution image (Fig. 4.3 d). The lattice spacing of the $\{10\bar{1}0\}$ and $\{11\bar{2}0\}$ planes are ~0.28 and ~0.16 nm, in agreement with the reported values for $MoSe_2$.[40]

Raman spectroscopy was carried out on a region containing 1 to 5 layers and thicker (bulk) domains (Fig. 4.4 b). The most prominent and identifiable peak is the out-of-plane A_{1g} mode located at 243.7 cm^{-1} for bulk $MoSe_2$, in agreement with literature.[34,33,37,38] We notice a softening of the A_{1g} mode from 243.7 cm^{-1} for bulk $MoSe_2$ to 241.2 cm^{-1} for single layer $MoSe_2$

when thickness is reduced, consistent with previous reports.[32,37,38] The monolayer $MoSe_2$ has a softening of the A_{1g} mode due to a decreasing interplanar restoring force. As expected, the interplanar restoring force is much stronger for thicker $MoSe_2$ samples from additional layers.[47] Thus, the $MoSe_2$ Raman mode blueshifts as the thickness increases (Fig. 4.4 a, d). The peak intensity is strongest for bilayer, and drops sharply for each additional layer (Fig. 4.4 a, c). The thickness dependent intensity could be due to optical enhancement, which was suggested in a previous report on MoS_2.[47] The dual peaks at layer numbers 3 – 5 (Fig. 4.4 a) is the effect of Davydov splitting, which results from the increasing number of $MoSe_2$ species per unit cell of the A_{1g} mode.[37]

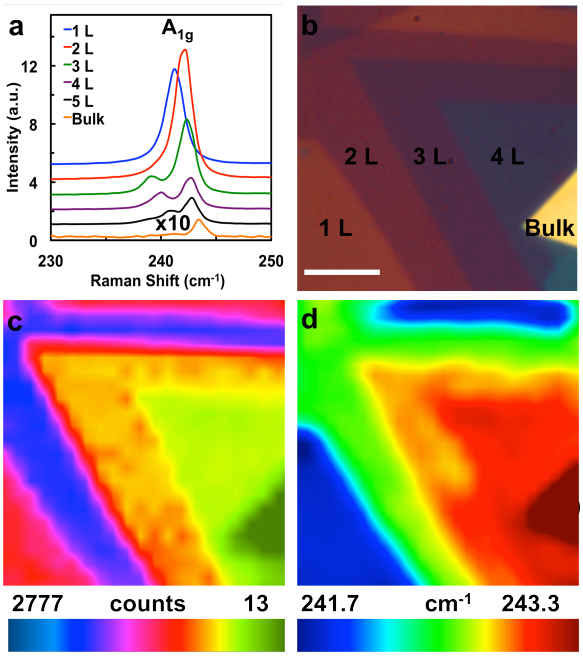

Figure 4.4 (a) Raman spectra of $MoSe_2$ with varying number of layers; the bulk spectrum is displayed 10x. **(b)** Corresponding optical micrograph for Raman mapping in (c, d), the scale-bar is 6 μm. **(c)** Raman map of overall intensity of the spectrum. **(d)** Raman map of the A_{1g} mode displaying a thickness-dependent mode shift.

The photoluminescence (PL) spectroscopy is arguably one of the most direct methods for assessing the band gap of monolayer TMDs.[39] It is well known that bulk $MoSe_2$ has an indirect

band gap of 1.1 eV.[8-10] However, recent theoretical and experimental studies have shown that monolayers should exhibit a direct band gap of 1.55 eV.[10,32,37,38] Our PL studies on monolayer $MoSe_2$ show a prominent emission peak at 800 +/- 5 nm, confirming the direct band gap of monolayer $MoSe_2$ at 1.55 +/- 0.01 eV (blue line in Fig. 4.5a). The PL intensity for the bilayer region is significantly reduced, by a factor of 35 (red line in Fig. 4.5a), compared to its monolayer counterpart. In addition, the florescence is red-shifted to 825 +/- 5 nm (1.50 +/- 0.01 eV). There is no noticeable peak for the trilayer PL (green line in Fig. 4.5a), as with increasing layer numbers the $MoSe_2$ transitions from a direct to an indirect band gap. PL mapping provides visual evidence the monolayer region exhibits much stronger emission compared with the bilayer region (Fig. 4.5 b, c). [10,32,37,38]

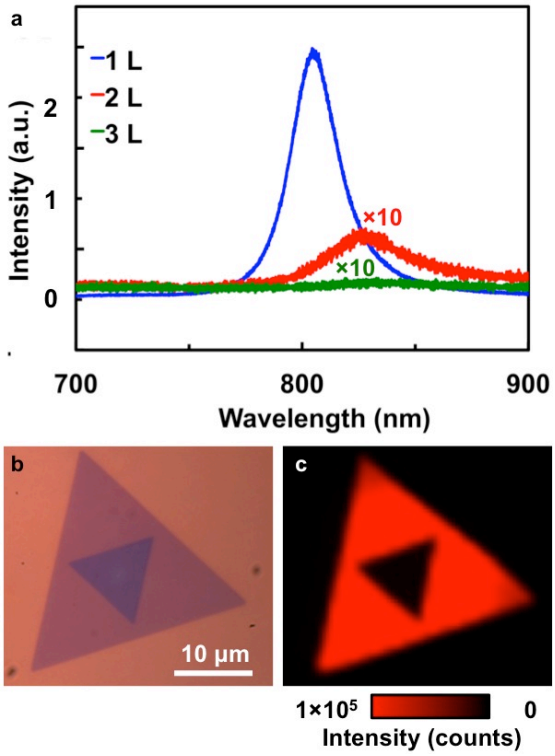

Figure 4.5 (a) Photoluminescence (PL) spectrum of one, two and three layers of $MoSe_2$ using 514 nm continuous laser with a 100x objective lens. **(b)** Optical micrograph of a $MoSe_2$ mono/bilayer crystal on a 300 nm SiO_2/Si substrate. **(c)** PL intensity map of (b).

4.4 Conclusion

We have synthesized large area $MoSe_2$ nanosheets using MoO_3 and Se powder precursors in a mixture of Ar and H_2 gases in a horizontal tube furnace. H_2 is a critical component of the reaction by enhancing the reduction of MoO_3 with Se to form $MoSe_2$. This first report of monolayer synthesis of $MoSe_2$ using CVD enables the growth directly on SiO_2/Si substrates. The triangular single-crystals are characterized by TEM and SAED. Thickness was determined using AFM and OM and then analyzed using Raman and PL spectroscopy, with characteristic peak shifts and a clear and indirect–direct band gap transition. This new synthesis of $MoSe_2$ expands our understanding in the growth of this and other 2D crystals and will enable researchers to further explore and engineer them into novel functional materials.

4.5 References

(1) Frindt, R. F.; Yoffe, A. D. Physical Properties of Layer Structures – Optical Properties and Photoconductivity of Thin Crystals of Molybdenum Disulfide. *Proc. R. Soc. London A,* **1969**, *273*, 69-83.

(2) Margulis, L.; Salitra, G.; Talianker, M.; Tenne, R. Nested Fullerene-like Structures. *Nature,* **1993**, *365*, 113-114.

(3) Prins, R.; De Beer, V. H. J.; Somorjai, G. A. Structure and Function of the Catalyst and the Promoter in Co-Mo Hydrodesulfurization Catalysis. *Catal. Rev. Sci. Eng.,* **1989**, *31*, 1.

(4) Karunadasa, H. I.; Montalvo, E.; Sun, Y. J.; Majda, M.; Long, J. R.; Chang, C. J. A Molecular MoS_2 Edge Site Mimic for Catalytic Hydrogen Generation. *Science,* **2012**, *335*, 698-702.

(5) Kim, Y.; Huang, J. L.; Lieber, C. M. Characterization of Nanometer Scale Wear and Oxidation of Transition-Metal Dichalcogenide Lubrications by Atomic Force Microscopy. *Appl. Phys. Lett.*, **1991**, *59*, 3404-3406.

(6) Li, Y.; Wang, H. L.; Xie, L. M.; Liang, Y.; Hong, G. S.; Dai, H. J. MoS2 Nanoparticles Grown on Graphene: An Advanced Catalyst for the Hydrogen Evolution Reaction. *J. Am. Chem. Soc.,* **2011**, *133*, 7296-7299.

(7) Huang, X.; Zeng, Z. Y.; Zhang, H. Metal dichalcogenide nanosheets: preparation, properties and applications. *Chem. Soc. Rev.*, **2013**, *42*, 1934.

(8) Kuc, A.; Zibouche, N.; Heine, T. Influence of quantum confinement on the electornic structure of the transition metal sulfide TS_2. *Physical Review B,* **2011**, *83*, 245213.

(9) Coehoorn, R.; Haas, C.; Dijkstra, J.; Flipse, C. J. F. Electronic Structure of MoSe2, MoS2 and WSe2, Band structure calculations and photoelectron spectroscopy. *Physical Review B,* **1987**, *35*, 15.

(10) Liu, L.; Kumar, S. B.; Ouyang, Y.; Guo, J.; Preformance limits of monolayer transition metal dichalcogenide transistiors. *IEEE Trans. Electron Devices*, **2011**, *58*, 3042-3047.

(11) Radisavljevic, B.; Radenovic, A.; Brivio, J.; Giacometti, V.; Kis, A. Single-layer MoS_2 transistors. *Nat. Nanotechnol.*, **2011**, *6*, 147-150.

(12) Sundaram, R. S.; Engel, M.; Lombardo, A.; Krupke, R.; Ferrari, A. C.; Avouris, Ph; Steiner M. Electroluminescence in single-layer MoS_2. *Nano Lett.*, **2013**, *13*, 1416-1421.

(13) Perkins, F. K.; Friedman, A. L.; Cobas, E.; Campbell, P. M.; Jernigan, G. G.; Jonker, B. T. Chemical Vapor Sensing with Monolayer MoS_2. *Nano Lett.,* **2013**, *13*, 668-673.

(14) Yin, Z. Y.; Li, H.; Li, H.; Jiang, L.; Shi, Y. M.; Sun, Y. H.; Lu, G.; Zhang, Q.; Chen, X. D.; Zhang, H. Single-layer MoS_2 phototransistors. *ACS Nano,* **2012**, *6*, 74-80.

(15) He, Q. Y.; Zeng, Z. Y.; Yin, Z. Y.; Li, H.; Wu, S. X.; Huang, X.; Zhang, H. Fabrication of Flexible MoS_2 Thin-Film Transistor Arrays for Practical Gas-Sensing Applications. *Small*, **2012**, *8*, 2994.

(16) Li, H.; Yin, Z. Y.; He, Q. Y.; Li, H.; Huang, X.; Lu, G.; Fam, D. W. H.; Tok, A. I. Y.; Zhang, Q.; Zhang, H. (2012), Fabrication of Single- and Multilayer MoS_2 Film-Based Field-Effect Transistors for Sensing NO at Room Temperature. *Small*, **2012**, *8*, 63–67.

(17) Zhu, C. F.; Zeng, Z. Y.; Li, H.; Li, F.; Fan, C. H.; Zhang, H. Single-Layer MoS_2-Based Nanoprobes for Homogeneous Detection of Biomolecules. *J. Am. Chem. Soc.,* **2013,** *135*, 5998-6001.

(18) Wu, J.; Li, H.; Yin, Z. Y.; Li, H.; Liu, J.; Cao, X.; Zhang, Q.; Zhang, H. Layer Thinning and Etching of Mechanically Exfoliated MoS_2 Nanosheets by Thermal Annealing in Air. *Small*, **2013**, *9*, 3314–3319.

(19) Lee, Y. H.; Zhang, X. Q.; Zhang, W. J.; Chang, T. M.; Lin, C. T.; Chang, K. D.; Yu, Y. C.; Wang, J. T. W.; Chang, C. S.; Li, L. J.; Lin, Y. W. Synthesis of large-area MoS2 atomic layers with chemical vapor deposition. *Adv. Mater.,* **2012**, *24*, 2320-2325.

(20) Zhan, Y. J.; Liu, Z.; Najmaei, S.; Ajayan, P. M.; Lou, J. Large Area Vapor Phase Growth and Characterization of MoS_2 Atomic Layers on SiO_2 Substrate. *Small,* **2012**, *8*, 966-971.

(21) Liu, K. K.; Zhang, W. J.; Lee, Y. H.; Lin, Y. C.; Chang, M. T.; Su, C. Y.; Chang, C. S.; Li, H.; Shi, Y. M.; Zhang, H.; Lai, C. S.; Li, L. J. Growth of Large-Area and Highly Crystalline MoS_2 Thin Layers on Insulating Substrates. *Nano Lett.,* **2012**, *12,* 1538-1544.

(22) Lee, Y. H.; Yu, L.; Wang, H.; Fang W. J.; Ling, X.; Shi, Y. M.; Lin, C. T.; Huang, J. K.; Chang, M. T.; Chang, C. S.; Dresselhaus, M.; Palacios T.; Li, L. J.; Kong, J. Synthesis and Transfer of Single-Layer Transition Metal Disulfides on Diverse Surfaces. *Nano*

Lett., **2013**, *13*, 1852-1857.

(23) Van der Zande, A. M.; Huang, P. Y.; Chenet, D. A.; Berkelbach, T. C.; You, Y.; Lee, G. H.; Heinz, T. F.; Reichman, D. R.; Muller, D. A.; Hone, J. C. Grains and grain boundaries in highly crystalline monolayer molybdenum disulphide. *Nat. Mater.,* **2013***,* *12*, 554-561.

(24) Najmaei, S.; Liu, Z.; Zhou, W.; Zou X. L.; Shi, G.; Lei, S. D.; Yakobson, B. I.; Idrobo, J. C.; Ajayan, P. M.; Lou, J. Vapour Phase Growth and Grain Boundary Structure of Molybdenum Disulphide Atomic Layers. *Nat. Mater.,* **2013**, *12*, 754-759.

(25) Geim, A. K.; Grigorieva, I. V. Van der Waals Heterostructures. *Nature,* **2013**, *449*, 419-425.

(26) Pouzet, J.; Bernede J. C. MoSe2 thin-films synthesized by solid-state reactions between Mo and Se thin-films. *Revue Phys. Appl*., **1990**, *25*, 807-815.

(27) Peng, Y.; Meng, Z. Y.; Zhong, C.; Lu, J.; Yu, W. C.; Jia, Y. B.; Qian, Y. T. Hydrothermal synthesis and characterization of single-molecular-layer MoS_2 and $MoSe_2$. *Chem. Lett.*, **2001**, *30*, 772-773.

(28) Matte, H. S. S. R.; Plowman, B.; Datta, R.; Rao, C. N. R. Graphene analogues of layered metal selenides. *Dalton Trans*., **2011**, *40*, 10322-10325.

(29) Kong, D. S.; Wang, H. T.; Cha, J. J.; Pasta, M. Koski, K. J.; Yao, J. Cui, Y. Synthesis of MoS2 and MoSe2 Films with Vertically Aligned Layers. *Nano Lett.,* **2013**, *13* 1341-1347.

(30) Jager-Waldau, A.; Lux Steiner, M.; Jager-Waldu, R.; Burkhardt, R.; Bucher, E.; *Thin Solid Films,* **1990**, 189, 339-345.

(31) Boscher, N. D.; Carmalt, C. J.; Palgrave, R. G.; Gil-Tomas, J. J.; Parkin, I. P. Atmospheric pressure CVD of molybdenum diselenide films on glass. *Chem. Vapor. Depos*., **2006**, *12*, 692-698.

(32) Tongay, S.; Zhou, J.; Ataca, C.; Lo, K,; Matthews, T. S.; Li, J. B.; Grossman, J. C.; Wu, J. Q. Thermally driven crossover from indirect toward direct bandgap in 2D semiconductors: $MoSe_2$ versus MoS_2. *Nano Lett.,* **2012**, *12*, 5576-5580.

(33) Larentis, S.; Fallahazad, B.; Tutuc, E. Field-effect transistors and intrinsic mobility in ultra-thin $MoSe_2$ layers. *Appl. Phys. Lett.,* **2012**, *101*, 223104.

(34) Kang, J.; Tongay, S.; Zhou, J.; Li, J. B.; Wu, J. Q. Band offsets and heterostructures of two-dimensional semiconductors. *App. Phys. Lett.,* **2013**, *102*, 012111.

(35) Li, X. S.; Magnuson, C. W.; Venugopal, A.; Tromp, R. M.; Hannon J. B.; Vogel, E. M.; Colombo, L.; Ruoff, R. S. Large-area graphene single crystals grown by low-pressure chemical vapor deposition of methane on copper. *J. Am. Chem. Soc.,* **2011**, *21*, 108-112.

(36) Peng, H.; Dang, W.; Cao, J.; Chen, Y. L.; Wu, D.; Zheng, W. S.; Li, H.; Shen, Z. X.; Liu, Z. F. Topological insulator nanostructures for near-infared transparent flexible electrodes. *Nat. Chem.,* **2012***, 4*, 281-286.

(37) Tonndorf, P.; Schmidt, R.; Böttger, P.; Zhang, X.; Börner, J.; Liebig, A.; Albrecht, M.; Kloc, C.; Gordan, O.; Zhan, D. R.; Michaelis de Vasconcellos, S.; Bratschitsch, R. Photoluminescence emission and Raman response of monolayer MoS_2, $MoSe_2$, and WSe_2. *Opt. Express,* **2013**, *4*, 4908-4916.

(38) Horzum, S.; Sahin, H.; Cahangirov, S.; Cudazzo, P.; Rubio, A.; Serin, T.; Peeters, F. M. Phonon softening and direct to indirect band gap crossover in strained single-layer $MoSe_2$. *Physical Review B,* **2013**, *87*, 6195.

(39) Splendiani, A.; Sun, L.; Zhang, Y. B.; Li, T. S.; Kim, J. H.; Chim, C. Y.; Galli, G.; Wang, F. Emerging photoluminesence in monolayer MoS_2. *Nano Lett.*, **2010**, *10*, 1271-1275.

(40) James, P. B.; Lavik, M. T. The crystal structure of $MoSe_2$. *Acta. Cryst*. **1963**, *16*, 1183.

(41) Huang, J. K.; Pu, J.; Chuu, C. P.; Hsu, C. L.; Chiu, M. H.; Juang, Z. Y.; Chang, Y. H.; Chang, W. H; Iwasa, Y.; Chou M. Y.; Large-area and highly crystalline WSe_2 monolayers : From synthesis to device applications. preprint athttp://arxiv.org/abs/1304.7365 .

(42) Zhang, Y.; Zhang, Y. F.; Ji, Q. Q.; Ju, J.; Yuan, H. T.; Shi, J. P.; Gao, T.; Ma, D. L.; Liu, M. X.; Chen, Y. B.; Song, X. J.; Hwang, H. Y.; Cui, Yi.; Liu, Z. F. Controlled Growth of High-Quality Monolayer WS_2 Layers on Sapphire and Imaging Its Grain Boundary. *ACS Nano,* **2013**, ASAP.

(43) Loginova, E.; Bartelt, N. C.; Feibelman, P. J.; McCarty, K. F. Evidence for graphene growth by C cluster attachment. *New J. Phys*., **2008**, *10*, 09026.

(44) Li, X. L.; Li, Y. D. Formation MoS_2 inorganic fullerenes (IFs) by the reaction of MoO_3 nanobelts and S. *Chem. Eur. J*., **2003**, *9*, 2726-2731.

(45) Zhou, H. Q.; Yu, F.; Liu, Y. Y.; Zou, X. L.; Cong, C. X.; Qiu, C. Y.; Yu, T.; Yan, Z.; Shen, X. N.; Sun, L. F.; Yakobson, B. I.; Tour, J. M. Thickness-dependent patterning of MoS_2 sheets with well-oriented triangular pits by heating in air. *Nano Res*., **2013**, *6*, 703-711.

(46) Liang, T.; Sawyer, W. G.; Perry, S. S.; Sinnott, S. B.; Phillpot, S. R. First-principles determination of static potential energy surfaces for atomic friction in MoS_2 and MoO_3. *Phys. Rev. B,* **2008**, *77*, 104105.

(47) Lee, C. G.; Yan, H.; Brus, L. E.; Heinz, T. F.; Hone, J.; Ryu, S. M. Anomalous Lattice

Vibrations of Single- and Few-Layer MoS_2. *ACS Nano.* **2010,** *4*, 2695-2700

Chapter 5. Alternate synthesis method to yield WSe_2 monolayer domains and films

5.1 Introduction

Graphene has attracted considerable interest for applications in diverse electronic and optoelectronic devices.[1-12] Despite the superior electronic properties of graphene, the gapless band structure limits the practical progress of graphene for digital electronic devices.[2,4] Recently, the energy band structures of the emerging transition metal dichalcogendes show the surprising indirect-to-direct band gap transition as their atomic layer number lowering to one.[13-18] For example, bulk WSe_2 is a p-type semiconductor with an indirect band gap of 1.2 eV, whereas its monolayer exhibits a direct band gap of 1.6 eV due to quantum confinement.[16,19] The direct band gap of atomically thin transition metal dichalcogendes benefits their applications on both digital electronic and optoelectronic devices.[20-24] A high performance p-type field-effect transistor (FET) fabricated on exfoliated single layered WSe_2 was demonstrated, making it a promising material for building atomically thin electronic and optoelectronic devices.[25] However, a large-area WSe_2 monolayer film is still a challenge for these promising applications, and the size of the monolayer obtained from mechanical exfoliation method is limited in a few to a few tens of micrometers.

In this chapter, an alternative synthetic strategy is reported for the preparation of single crystal WSe_2 single-layers directly on 300 nm SiO_2/Si substrates by chemical vapor deposition. This technique can produce large area samples using a growth process applying several growth parameters. The areal size of the as-grown monolayer WSe_2 film is as large as 1 cm^2 with optical and electronic properties comparable to exfoliated samples. Both transmission electron microscopy (TEM) and photoluminescence (PL) are performed on the same single crystal WSe_2 single-layer crystal, allowing us to directly correlate structural and optical properties with

resolution down to the atomic level. Additionally, the successful preparation of WSe_2 crystals provides an ideal platform for fabricating atomically thin p-type electronic devices.

5.2 Methods

To synthesize monolayer WSe_2, 0.2 g WSe_2 powder (Alfa Aesar) was added into an alumina boat and placed at the center of the furnace (Fig. 5.1). The blank 300 nm SiO_2/Si substrates (1 cm x 5 cm) loaded into a home-built vapor deposition system in a horizontal tube furnace (Lindberg/Blue M) with 1-inch quartz tube. The system was pumped down to a vacuum of 10 mTorr in 10 min, and re-filled with 150 sccm of ultra-high purity argon gas (Airgas, ~ 99.9999%) then heated to desired growth temperature within 30 min. Next, the growth kept at the designed temperature for 30 min, and then terminated by shutoff the power of the furnace. The sample was naturally cooled down to ambient temperature.

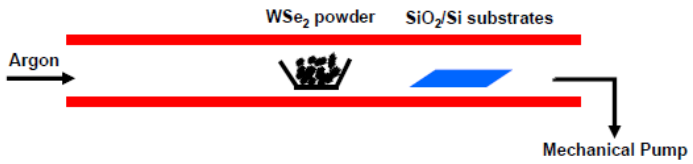

Figure 5.1. Schematic illustration of the CVD growth equipment and temperature growth recipe. The WSe_2 powders are placed in an alumina boat at the center of the quartz tube. The SiO_2/Si substrates are placed in downstream region of the tube furnace. Ar is continuously supplied through the reactor.

5.3 Results and Discussion

Single and few-layer WSe_2 grew in triangular single layers, similarly to previous TMD nanosheet growth (Fig. 5.2b). The lower growth temperature typically results in a higher density of thermally induced nucleation, and a higher flow rate of the carrier gas introduces the similar effect due to the consequently higher supersaturation of the precursors. On the other hand, the higher growth temperature and flow rate stimulates the nucleation of the extra molecular layers. At lower growth temperature of 1060 °C with low flow rate of 100 sccm, there is no WSe_2

islands observed on the SiO_2/Si substrates using optical microscope (OM). By increasing the growth temperature to 1065 °C, the monolayer WSe_2 domains (~ 10 μm of average edge size) are observed with nucleation density of ~ 1060/mm^2 (Fig. 5.2b). When the growth temperature is 1070 °C, the bilayer WSe_2 domains (~ 20 μm of average edge size) are observed with the lower domain density of ~ 350/mm^2. The thicker flakes (~ 50 μm of average edge size) appear as the growth temperature increased to 1075 °C with even lower domain density of ~ 280/mm^2 (Fig. 5.2e). Overall, higher growth temperature yields a lower density of thicker WSe_2 nanosheets with a larger domain size. By increasing the flow rate of the carrier gas, both the thickness and the domain density of the WSe_2 are increased. For instance, at growth temperature of 1065 °C, nucleation density of ~ 1060/mm^2 is observed under 100 sccm flow rate of carrier gas. That is increased to ~ 11000/ mm^2 under 150 sccm, and ~ 23000/ mm^2 under 200 sccm, which is clearly support our conclusion. Figure 5.2 contains OM images, which summarize all the growth conditions with alternating temperature and flow rate. All of our observations are consistent with the nucleation model of the vapor phase deposition developed

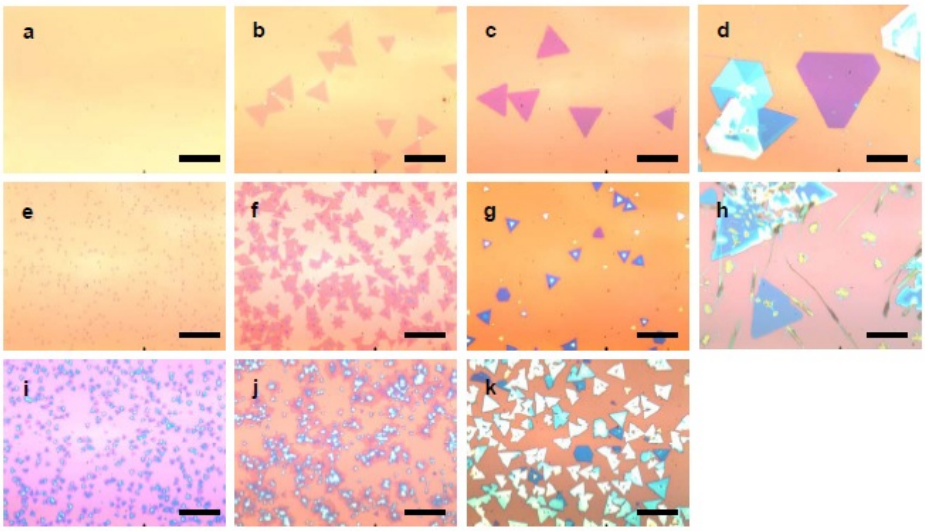

Figure 5.2. Reactor conditions depicting WSe_2 growth with varying temperature and flow-rates. Optical microscope images of WSe_2 samples grown at different temperature under designed flow rate for 20 min **(a)** 1060 °C, 100 sccm; **(b)** 1065 °C, 100 sccm; **(c)** 1070 °C, 100 sccm; **(d)** 1075 °C, 100 sccm; **(e)** 1060 °C, 150 sccm; **(f)** 1065 °C, 150 sccm; **(g)** 1070 °C, 150 sccm; **(h)** 1075 °C, 150 sccm; **(i)** 1060 °C, 200 sccm; **(j)** 1065 °C, 200 sccm; **(k)** 1070 °C, 200 sccm. All the scale bars are 20 μm.

by W. K. Burton and N. Cabrera, where they predict that the nucleation probability is proportional to supersaturation and 1/T formation.[26]

An OM image of the triangular shaped WSe_2 monolayer domain grown at 1065 °C (Fig. 5.3a**)**. The PL emission spectrum from monolayer WSe_2 shows peak at ~ 766 nm (Fig. 5.3c), which is consistent with the previous reports on exfoliated WSe_2 monolayers.[14,15] Uniform and strong emission intensity is observed in the PL mapping images (Figure 5.3b), indicating that the WSe_2 exhibits a high crystal quality and uniformity. The average edge length of a triangular WSe_2 single-layer crystal after 20 minutes growth is shown to be 5 μm by OM (Fig. 5.3d). With longer growth time (30 min), the monolayer domains starts to merge together, with bilayer and few-layer domains occasionally appeared on their first layer (Fig. 5.3e**)**. After 40 min growth, the WSe_2 monolayer domains are coalesced, and additional crystal layers can be distinguished due to optical contrast (Fig. 5.3f). OM can be used to distinguish the WSe_2 thickness on a large scale. The corresponding atomic force microscopy (AFM) (Fig. 5.3g) shows the thickness of the second layer is ~ 0.7 nm, which is in agreement with the reported value for mechanically exfoliated WSe_2 layers.[14,15] The lateral size of the as-grown monolayer WSe_2 film is as large as 1 cm^2 (Fig. 5.3h), and the transferred WSe_2 film on the glass is shown to be transparent (Fig. 5.3i).

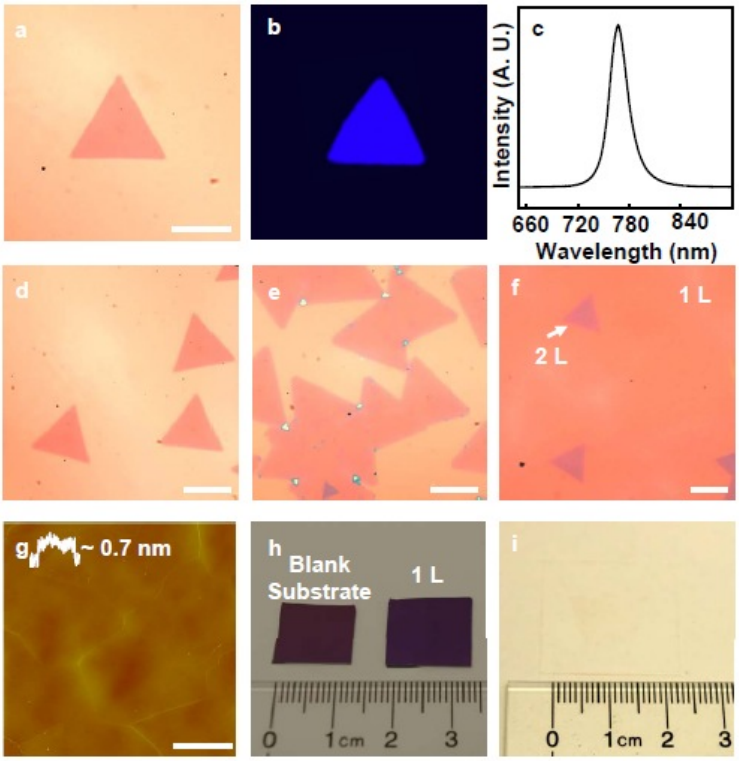

Figure 5.3. (a) A typical optical microscope (OM) image of a single-layer WSe_2 nanosheet on a 300 nm SiO_2/Si substrate. **(b)** Photoluminescence (PL) map (766 nm) of the single-layer WSe_2 sample shown in (a). **(c)** PL spectrum taken from (a). **(d)** OM image of single-layer WSe_2 nanosheets taken after 20 minutes of growth, **(e)** after 30 minutes of growth and **(f)** after 40 minutes of growth. **(g)** Atomic force microscopy image taken on the same region as shown in (f). **(h)** Photograph of the ~1 cm^2 size single-later WSe_2 film obtained with 40 minute growth time. **(i)** Photograph of the ~1 cm^2 sized single-layer WSe2 film transferred onto a glass slide. All scale bars are 5 μm.

Raman spectroscopy, PL, and AFM are employed to study the monolayer/bilayer WSe_2 domains. The monolayer WSe_2 domain is triangular, with the bilayer region crystalizing from the center of their first layer (Fig. 5.4a). The corresponding Raman map can be further used to distinguish the number of layers of the WSe_2 domains (Fig. 5.4b). The darker triangular region on the Raman map corresponds to the bilayer WSe_2 domain. Nearly same color contrast throughout the monolayer and bilayer area indicates a uniform crystal quality. The Raman spectra of WSe_2 show typical features of active A_{1g} (~ 250 cm^{-1}) and inactive B_{2g} (~ 307 cm^{-1})

modes. In general, the B_{2g} signature only is active on the bilayer area, which could reflect the presence of the additional interlayer interaction.[14,15] In contrast, the Raman A_{1g} mode of WSe_2 is less sensitive to layer thickness, where the peak is located at 252 cm^{-1}. The Raman intensity of A_{1g} mode decreases with atomic layer thickness. Similarly, the peak intensity recorded by the PL rapidly decreases with the number of layers increasing (Fig. 5.4f). The PL peaks of the as-grown WSe_2 monolayer and bilayer are located at approximately 766 and 788 nm, respectively, with full-width-half-maximum (FWHM) values of 23 and 68 meV, which is comparable to the published data of exfoliated WSe_2.[14,15] The dark region of the PL map clearly highlights the lack of emission in the second layer of WSe_2 (Fig. 5.4c). This result strongly indicates the high crystal quality of the as-grown WSe_2 atomic layers. The number of WSe_2 molecular layers is also determined by AFM measurements (Fig. 5.4d). The AFM step heights of WSe_2 monolayer on the SiO_2 substrate is typically measured between 0.7 – 1.0 nm, and the step heights of bilayer on monolayer amount to ~ 0.7 nm (line scan in Fig. 5.2d), which is consistent with the published reports of exfoliated WSe_2.[15]

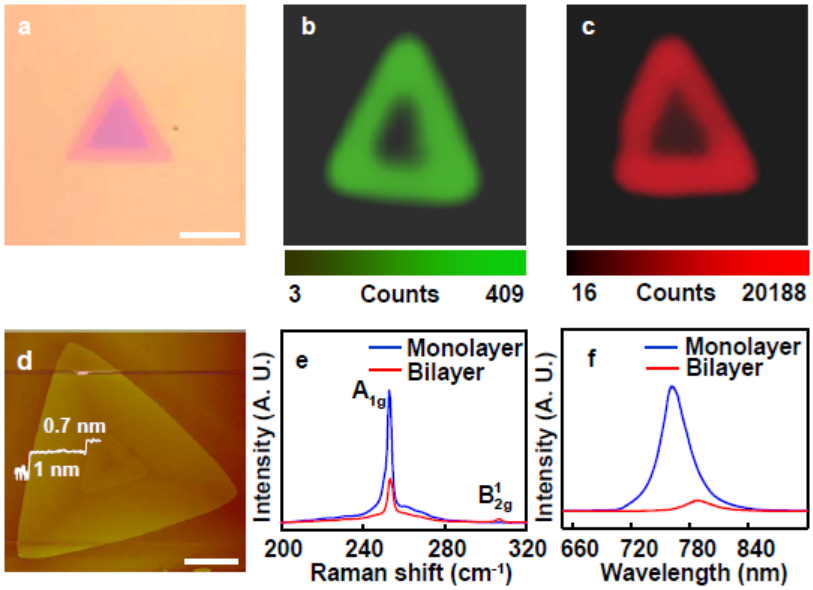

Figure 5.4. **(a)** Optical microscope (OM) image of a monolayer WSe_2 nanosheet with an optically distinguishable bilayer domain in the center. **(b)** Raman map (250 cm^{-1}) of (a). **(c)** PL map (766 nm) of (a). **(d)** Atomic force microscopy image of a monolayer WSe_2 nanosheet with a bilayer domain at the center of the crystal. **(e)** The Raman spectra of the monolayer and bilayer WSe_2. **(f)** PL spectra of monolayer and bilayer WSe_2. The scale bars are 5 μm.

After 40 min growth at temperature of 1065 °C under 100 sccm of Ar carrier gas, the triangular monolayer WSe_2 domains continue to grow and merge to form films. The SiO_2/Si substrates are completely covered by the monolayer WSe_2 domains with less than 5% areal coverage of the bilayer (Fig. 5.5a). We then further studied the completely covered monolayer WSe_2 samples by the PL mapping and AFM (Fig. 5 b, c). PL mapping measurement can be used to identify the layer numbers of the WSe_2 films. The PL spectra of the monolayer region show the identified peak at 766 nm (blue color spectrum in Fig. 5.5d), the uniform color contrast and strong light emission from monolayer indicates the high quality of the completely covered WSe_2 films. The darker triangular area on the OM image corresponds to the bilayer WSe_2 (5.5a). A typical spectrum (red color spectrum in Fig. 5.5d) of bilayer WSe_2 shows a wider peak at 790 nm with significantly lower intensity. Within the PL mapping region (~ 100 × 100 μm), the uniform

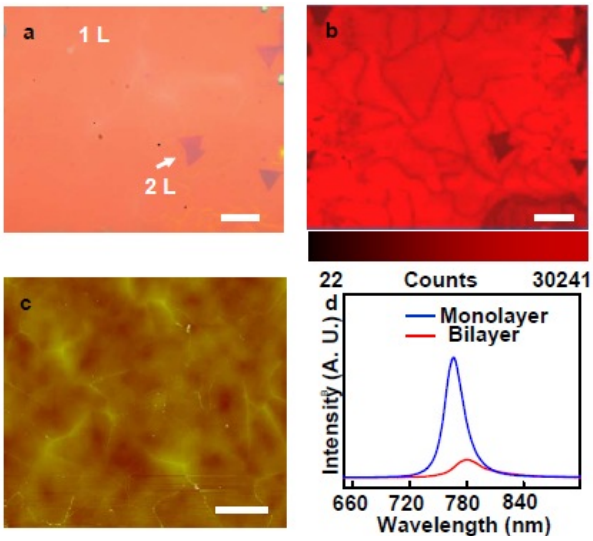

Figure 5.5. **(a)** Optical microscope (OM) image of fully covered WSe_2 on 300 nm SiO_2/Si substrates with the bilayer region highlighted. **(b)** PL map of the fully covered WSe_2 in (a). **(c)** AFM image of the fully covered monolayer WSe_2 in (a). **(d)** PL spectra taken from the marked areas in (b). Scale bars are 10 μm.

PL peak heights observed throughout the scanning area indicate high crystal quality and uniformity of the monolayer WSe_2 films. The dark lines in the PL map indicate the grains from which the WSe_2 nanosheets merged together. The PL mapping and corresponding AFM confirms the 100% large area monolayer WSe_2 films coverage.

The as-prepared WSe_2 atomic layers on 300 nm SiO_2/Si substrate can be transferred onto arbitrary substrates by etching away the SiO_2 layer using buffer oxide etching (BOE) solution. The released WSe_2/PMMA films are seen floating on the surface of DI water that was removed from its original growth substrate (Fig. 5.6a). The area of the WSe_2 sample is relies on the size of the substrates, suggesting that the process is scalable. The WSe_2 nanosheets can then be transferred onto arbitrary substrates for further characterizations and processing. Figure 5.6c shows a photo depicting the WSe_2 monolayer transferred onto a glass substrate, and Figure 5.6d shows the corresponding light transmittance spectra of WSe_2 monolayer. General features of the absorption peaks A and B, which arise from the direct band gap transitions are found around 760 and 600 nm, respectively.[27] The representative X-ray diffraction spectrum of large area WSe_2 monolayer confirms the hexagonal crystal structure (5.6e). The diffraction peak of around 33° can be assigned to the SiO_2/Si substrate. The spectrum of the WSe_2 monolayer only contains a broad

(002) peak indicating that the single crystals are in perfect (00*l*) orientation, which indicates the presence of crystallites with van der Waals' planes parallel to the substrate surface.

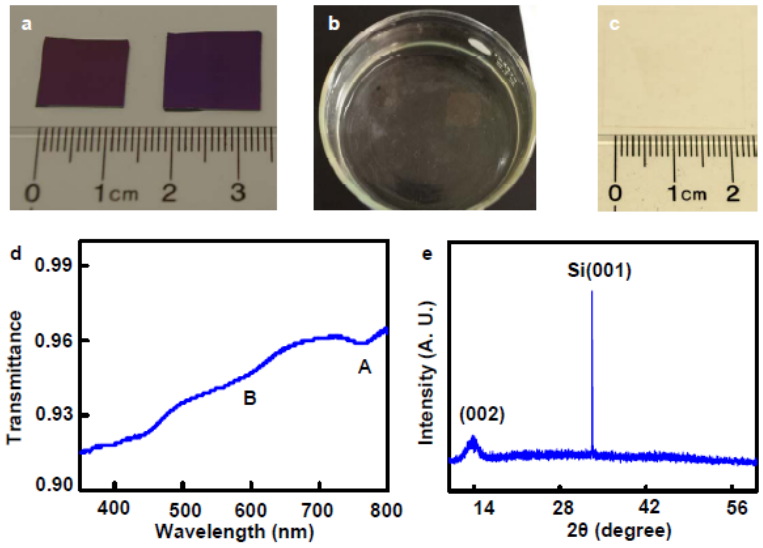

Figure 5.6. **(a)** Photograph of ~ 1cm^2 sized monolayer WSe_2 films obtained with 40 min growth time. **(b)** WSe_2/PMMA film floating on the surface of water. **(c)** Photograph of the same WSe_2 film from (a, b) transferred on a glass slide. **(d)** Light transmission spectrum of monolayer WSe_2 from (c). (e) X-ray diffraction spectra of monolayer WSe_2 film from (a).

In order to directly correlate the optical properties of the WSe_2 layered crystals to its atomic structure, we have performed transmission electron microscopy (TEM), electron diffraction (ED), and PL investigations on the same WSe_2 nanosheet. The as-grown WSe_2 nanosheet was transferred onto a holy carbon-coated TEM grid (Fig. 5.7a). A PL map of the WSe_2 nanosheet (Fig. 5.7b) shows the PL map of the same WSe_2 atomically thin crystal with light emission from monolayer, bilayer, and few-layer. The PL peaks at 788 nm and 766 nm respectively match the band gap energy of bi- and monolayer WSe_2 reported by exfoliated materials (Fig. 5.7c).[14, 15] No PL peak is found on multi-layered WSe_2 (>3 layers), and the recorded intensity of the bilayer peak is about 10 times lower than that of the monolayer peak,

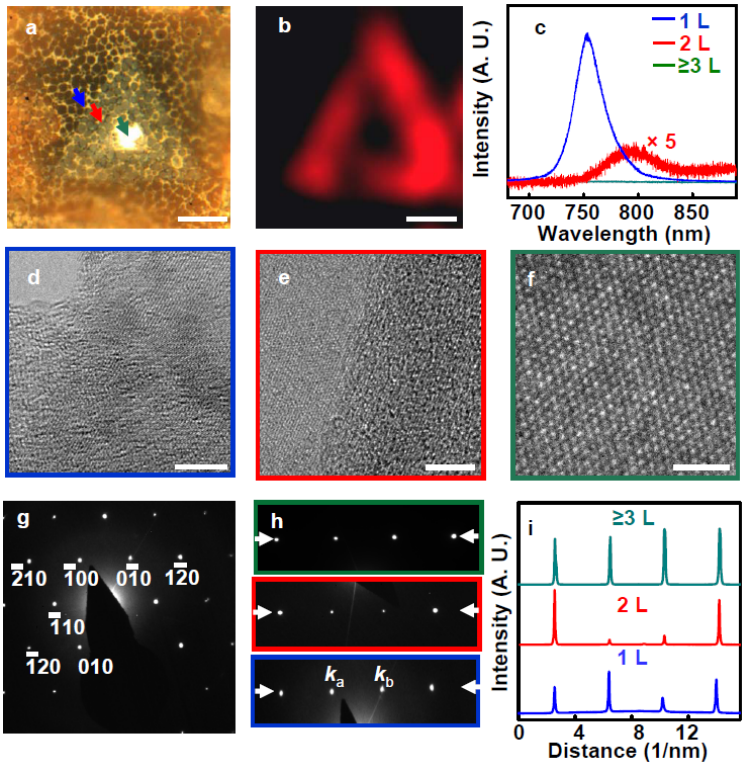

Figure 5.7. (a) Optical micrograph (OM) of a WSe_2 crystal with monolayer etches and a multilayered domain in the center. Scale bar is 10 µm. **(b)** Corresponding photoluminescence (PL) map of the WSe_2 sample shown in (a). **(c)** PL spectra of the WSe_2 nanosheet taken from areas of the monolayer, bilayer and multilayer from (a). **(d)** Bright-field high-resolution transmission electron microscopy (HRTEM) image of the WSe_2 sample, which is taken from the approximate location indicated by a blue arrow in (a). Scale bar is 5 nm. **(e)** HRTEM image taken from the approximate location indicated by the red arrow in (a). **(f)** HRTEM image taken from the approximate location indicated by the green arrow in (a). Scale bar is 2 nm**. (g)** Selected area electron diffraction (SAED) pattern taken from the area of monolayer WSe_2. **(h)** The SAED patterns between (10) and (1 0) enclosed with a blue, red and green lines from monolayer, bilayer and few layer WSe_2, respectively. **(i)** Profile plots of the diffraction peak intensities along the white arrows in (h).

which is consistent with the expected evolution of a direct-to-indirect band gap. These PL results confirm that the WSe_2 monolayer, bilayer and few layers on the same crystal domain. Therefore, the atomic layer numbers of the WSe_2 is confirmed by this PL measurement. In order to directly correlate the PL spectrum of the WSe_2 atomic layers to their lattice structure, PL and HRTEM are performed on the same WSe_2 nanosheet. Figures 5.7d to 5.7f show the images of the atomic structure of the WSe_2 monolayer, bilayer, and few layers, respectively. The representative HRTEM images from different layers are taken on selected regions (Fig. 5.7a). The hexagonal lattice is clearly visible from each atomic resolution image. The selected-area electron diffraction (SAED) is used to characterize the

crystal structure of the island. The SAED pattern of the monolayer WSe_2 with the zone axis of [0001], the six-fold symmetry in the position of the diffraction spots demonstrates that the triangular monolayer is predominantly single crystal with hexagonal structures (Fig. 5.7g). It's possible to identify the different atomic layer numbers using SAED. Figure 5.7h shows the four electron diffraction spots ($\bar{2}10$, $\bar{1}00$, $0\bar{1}0$, and $1\bar{2}0$) of WSe_2 monolayer, bilayer and few layers, respectively. The line profiles of the corresponding diffraction spots shown in Figure 5.7g are plotted in Figure 5.7h. The line profile of WSe_2 few layers show approximately the same intensity ratio of the outer {112} peak over the inner {110} peak, which is in good agreement with the previously reported bulk results.[28] In contrast, the average intensity ratio of the outer {112} peak over the inner {110} peak in the profile plots shows opposite trend for the monolayer and bilayer WSe_2, which is similar to the monolayer and bilayer graphene.[29, 30] In addition, similar to the Bloch wave simulations on monolayer MoS_2,[31] the monolayer W and Se sublattices reduce its hexagonal lattice from six-fold to three fold symmetry, which break the six [$\bar{1}00$] diffraction spots into two families (k_a ={($\bar{1}00$), ($1\bar{1}0$), (010)} and k_b =- k_a). We also observe the k_a spots are higher in intensity compared to k_b spots, which is a consistent observation with Ref. 25.

5.4 Conclusion

In summary, we have reported a method of vaporizing solid WSe_2 powder to synthesize WSe_2 monolayer, bilayer, and few-layer nanosheets. Through the characterization of atomic force microscopy, photoluminescence mapping, light transmission, and X-ray diffraction, we show that the large area transferable monolayer WSe_2 thin film with lateral dimensions approaching ~ 1 cm^2. We performed the transmission electron microscopy and micro-photoluminescence mapping on the same WSe_2 nanosheet, observing a clear intensity revolution

of the SAED pattern. The ability to synthesize atomically thin materials can open up entirely new possibilities for the design of future van de Waals heterostructures for electronic and photonic devices.

5.5 References

(1) Novoselov, K. S.; Fal'ko, V.; Colombo, I. L.; Gellert, P. R.; Schwab.M. G.; Kim, K. *Nature* **2012**, *490*, 192−200.

(2) Schwierz, F. *Nat. Nanotechnol.* **2010**, *5*, 487−496.

(3) Bonaccorso, F.; Sun, Z.; Hasan, T. A.; Ferrari, C. *Nat. Photon.* **2010**, *4*, 611−622.

(4) Weiss, N. O.; Zhou, H.; Liao, L.; Liu, Y.; Jiang, S.; Huang, Y.; Duan, X. *Adv. Mater.* **2012**, *24*, 5782−5825.

(5) Liao, L.; Lin, Y.-C.; Bao, M.; Cheng, R.; Bai, J.; Liu, Y.; Qu, Y.; Wang, K. L.; Huang, Y.; Duan, X. *Nature* **2010**, *467*, 305−308.

(6) Bao, Q.; Loh, K. P. *ACS nano* **2012**, *6*, 3677−3694.

(7) Lin, Y. M.; Valdes-Garcia, A.; Han, S.-J.; Farmer, D. B.; Meric, I.; Sun, Y.; Wu, Y.; Dimitrakopoulos, C.; Grill, A.; Avouris, P.; Jenkins, K. A. *Science* **2011**, *332*, 1294−1297.

(8) Britnell, L.; Britnell, L. R.; Gorbachev, V.; Jalil, R.; Belle, B. D.; Schedin, F.; Mishchenko, A.; Georgiou, T.; Katsnelson, M. I.; Eaves, L.; Morozov, S. V.; Peres, N. M. R.; Leist, J.; Geim, A. K.; Novoselov, K. S.; Ponomarenko, L. A. *Science* **2012**, *335*, 947−950.

(9) Yang, H.; Heo, J.; Park, S.; Song, H. J.; Seo, D. H.; Byun, K.-E.; Kim, P.; Yoo, I.; Chung,H.-J.; Kim, K. *Science* **2012**, *336*, 1140−1143.

(10) Xia, F.; Mueller, T.; Lin, Y. M. ; Valdes-Garcia, A.; Avouris, P. *Nat. Nanotechnol.* **2009**, *4*, 839−843.

(11) Liu, Y.; Cheng, R.; Liao, L.; Zhou, H.; Bai, J.; Liu, G.; Liu, L.; Huang, Y.; Duan, X. *Nat. Commun.* **2011**, *2*, 579.

(12) Mueller, T.; Xia, F.; Avouris, P. *Nat. Photon.* **2010**, *4*, 297−301.

(13) Splendiani, A.; Sun, L.; Zhang, Y.; Li, T.; Kim, J.; Chim, C.-Y.; Galli, G.; Wang, F. *Nano Lett.* **2010**, *10*, 1271−1275.

(14) Li, H.; Lu, G.; Wang, Y.; Yin, Z.; Cong, C.; He, Q.; Wang, L.; Ding, F.; Yu, T. Zhang, H. *Small* **2013**, *9*, 1974−1981.

(15) Tonndorf, P.; Schmidt, R.; Böttger, P.; Zhang, X.; Börner, J.; Liebig, A.; Albrecht, M.; Kloc, C.; Gordan, O.; Zahn, D. R. T.; de Vasconcellos, S. M.; Bratschitsch, R. *Optics Express* **2013**, *21*, 4908−4916.

(16) Terrones, H.; López-Urías, F.; Terrones, M. *Scientific Reports* **2013**, *3*, 1549.

(17) Lee, Y. H.; Yu, L.; Wang, H.; Fang, W.; Ling, X.; Shi, Y.; Lin, C. -T.; Huang, J. -K.; Chang, M. -T.; Chang, C. -S.; Dresselhaus, M.; Palacios, T.; Li, L. -J.; Kong, J. *Nano Lett.* **2013**, *13*, 1852−1857.

(18) Ji, Q.; Zhang, Y.; Gao, T.; Zhang, Y.; Ma, D.; Liu, M.; Chen, Y.; Qiao, X.; Tan, P. -H.; Kan, M.; Feng , J.; Sun, Q.; Liu, Z. *ACS Nano* **2013**, *13*, 3870−3877.

(19) Kumar, K.; Ahluwalia, P. K. *Eur. Phys. Journal B* **2012**, *85*, 186−192.

(20) Najmaei, S.; Liu, Z.; Zhou, W.; Zou, X.; Shi, G.; Lei, S.; Yakobson, B. I.; Idrobo, J. -C.; Ajayan, P. M.; Lou, J. *Nat. Mater.* **2013**, *12*, 754−759.

(21) Wang, Q. H.; Kalantar-Zadeh, K.; Kis, A.; Coleman, J. N.; Strano, M. S. *Nat. Nanotechnol.* **2012**, *7*, 699−712.

(22) Yu, W. J.; Liu, Y.; Zhou, H.; Yin, A.; Li, Z.; Huang, Y.; Duan, X. *Nat. Nanotech.* **2013**, *8*, 952−958.

(23) Yu, W. J.; Li, Z.; Zhou, H.; Wang, Y.; Huang, Y.; Duan, X. *Nat. Mater.* **2012**, *12*, 246−252.

(24) Zhu, C. F.; Zeng, Z. Y.; Li, H.; Li, F.; Fan, C. H.; Zhang, H. *J. Am. Chem. Soc.* **2013**, *135*, 5998−6001.

(25) Fang, H.; Chuang, S.; Chang, T. C.; Takei, K.; Takahashi, T.; Javey, A. *Nano Lett.* **2012**, *12*, 3788−3792.

(26) Burton, W. K.; Cabrera, N.; *Discussions Faraday Soc.* **1949**, *5*, 33−39.

(27) Zhao, W.; Ghorannevis, Z.; Chu, L.; Toh, M.; Kloc, C.; Tan, P. -H.; Eda, G. *ACS Nano* **2013**, *7*, 791−797.

(28) Khelil, A.; Essaidi, H.; Bernede, J. C.; Bouacheria, A.; Pouzet, J. *J. Phys.: Condens. Matter* **1994**, *6*, 8527−8537.

(29) Liu, L.; Zhou, H.; Cheng, R.; Yu, W. J.; Liu, Y.; Chen, Y.; Shaw, J.; Zhong, X.; Huang, Y.; Duan, X. *ACS Nano* **2012**, *6*, 8241−8249.

(30) Zhou, H.; Yu, W. J.; Liu, L.; Cheng, R.; Chen, Y.; Huang, X.; Liu, Y.; Wang, Y.; Huang, Y.; Duan, X. *Nat. commun.* **2013**, *4*, 2096.

(31) van der Zande, A. M.; Huang, P. Y.; Chenet, D. A.; Berkelbach, T. C.; You, Y.; Lee, G. -H.; Heinz, T. F.; Reichman, D. R.; Muller, D. A.; Hone, J. C. *Nat. Mater.* **2013**, *12*, 554−561.

(32) Liu, L.; Kumar, S. B.; Ouyang, Y.; Guo, J. *IEEE Trans. Electron Devices* **2011**, *58*, 3042−3047.

(33) Lee, Y. H.; Zhang, X. Q.; Zhang, W. J.; Chang, T. M.; Lin, C. T.; Chang, K. D.; Yu, Y. C.; Wang, J. T. W.; Chang, C. S.; Li, L. J.; Lin, Y. W. *Adv. Mater.* **2012**, *24*, 2320−2325.

(34) Huang, X.; Zeng, Z.; Zhang, H. *Chem. Soc. Rev.* **2013**, *42*, 1934−1946.

(35) Zhan, Y. J.; Liu, Z.; Najmaei, S.; Ajayan, P. M.; Lou, J. *Small* **2012**, *8*, 966−971.

(36) Liu, K. K.; Zhang, W. J.; Lee, Y. H.; Lin, Y. C.; Chang, M. T.; Su, C. Y.; Chang, C. S.; Li, H.; Shi, Y. M.; Zhang, H.; Lai, C. S.; Li, L. J. *Nano Lett.* **2012**, *12*, 1538−1544.

(37) Larentis, S.; Fallahazad, B.; Tutuc, E. *Appl. Phys. Lett.* **2012**, *101*, 223104.

Chapter 6. Synthesis strategy to produce MoS_2-$MoSe_2$ and WS_2-WSe_2 vertical and lateral heterostructures

6.1 Introduction

Inspired by the recent advancements in graphene, the layered transition metal dichalcogenides (TMDs) (*e.g.* MoS_2, $MoSe_2$, WS_2 and WSe_2) have attracted considerable attention as two-dimensional (2-D) semiconductors with unique layer-number dependent electronic and optical properties[1-22]. Exploring the full potential of these layered semiconductors requires precise spatial modulation of the chemical, structural and electronic properties in these 2-D atomic crystals to create well-defined heterostructures. Traditional semiconductor heterostructures have essentially defined the foundation of all modern electronic and optoelectronic devices, including transistors, p-n diodes, photovoltaic/photodetection devices, light-emitting diodes and laser diodes. Although the graphene-boron nitride (h-BN) based 2-D lateral heterostructures has been reported[23-26], the growth of TMD lateral heterostructures is of considerable challenge and had not been realized until 2014, despite the increasing efforts on the growth of diverse TMD nanosheets[27-40].

In this chapter, compositionally modulated MoS_2-$MoSe_2$ and WS_2-WSe_2 lateral and vertical heterostructures have been prepared by *in situ* modulating the vapor phase reactants during growth of these 2D crystals. Raman and photoluminescence mapping studies demonstrate the resulting heterostructure nanosheets exhibit clear structural and optical modulation. Transmission electron microscopy and electron diffraction studies reveal a single crystalline structure, and the energy dispersive x-ray elemental mapping confirms spatial modulation of chemical compositions in the heterostructure nanosheets.

It has been recently shown, both in this thesis and in the scientific community, that a wide range of TMD materials (e.g. MoS_2, $MoSe_2$, WS_2, WSe_2) can be directly grown on a silicon oxide substrate in the form of single or few-layered nanosheets or well-faceted triangular or hexagonal domains[27-40]. The synthetic process usually involves a thermal chemical vapor deposition (CVD) process, in which the vapor phase reactantants are generated by thermally evaporating the selected solid source material. With this approach, heterostructures can in principle be produced through successive growth of a second material (e.g., $MoSe_2$, WSe_2) at the edge of an existing domain of a first material (e.g., MoS_2, WS_2). With a relatively small lattice mismatch (~4 %) between MoS_2 and $MoSe_2$ or WS_2 and WSe_2, it is possible to produce coherent MoS_2-$MoSe_2$ and WS_2-WSe_2 heterostructures through a vertical and lateral epitaxial process (Fig. 5.1a). Although conceptually simple, the growth of TMD lateral heterostructures is of considerable challenge. Our studies indicate simple sequential growth often failed to produce the desired heterostructures because: (1) the edge growth front can be easily passivized after the termination of the first growth and exposure to ambient conditions, and cannot function as the effective nucleation site for subsequent lateral epitaxial growth after transferred into a second growth chamber; and (2) the atomically thin TMD nanosheets are usually too delicate (e.g., far more volatile than graphene or BN) to withstand significant changes in growth temperature or conditions[41] that are often necessary for the sequential growth of a second material to form the desired heterostructures.

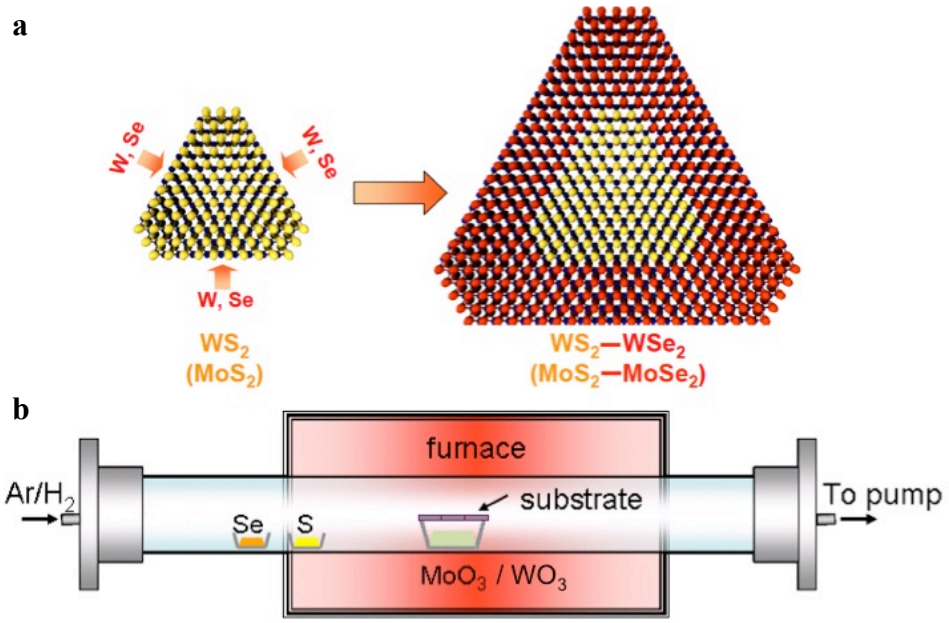

Figure 6.1. (a) A triangular domain of WS_2 (MoS_2) is first grown using a chemical vapor deposition process. The peripheral edges of the triangular domain features unsaturated dangling bonds that function as the active growth front for the continued addition and incorporation of precursor atoms to extend the two dimensional crystal in the lateral direction. With an *in situ* switch of the chemical vapor source for WSe_2 ($MoSe_2$) during middle of the growth, lateral hetero-epitaxial growth can occur at the peripheral active growth front to form WS_2-WSe_2 (MoS_2-$MoSe_2$) lateral heterostructures. **(b)** The MoO_3/WO_3 powder and elemental S and Se powders were used as the solid source. The MoO_3/WO_3 powder is kept in the center hot zone, and the S and Se vapor was sequentially introduced into the CVD reaction by shifting quartz tube rightward to move the S and Se source into the furnace without breaking vacuum.

6.2 WS_2-WSe_2 lateral heterostructures

To grow lateral heterostructures, it is therefore essential to design similar synthetic conditions applicable for both materials of interest and to retain a fresh, un-passivized edge growth front for successive lateral epitaxy. To this end, we have designed a thermal CVD process (Fig. 6.1b) that can allow *in situ* switch of the vapor phase reactants to enable lateral epitaxial growth of single or few-layered TMD lateral heterostructures. For example, to produce a WS_2-WSe_2 heterostructure (Fig. 6.2a), the WS_2 domains are first grown in a CVD process using previously described methods; WO_3 power is sprinkled on-top of substrates at the center of the heating zone, while S powder is placed in a alumina boat upstream and outside of the hot

zone. The entire CVD process occurs in a 1-inch tube furnace in an argon atmosphere (Fig. 6.1b). The peripheral edges of the triangular domains feature unsaturated dangling bonds that function as the active growth front for the continued addition and incorporation of precursor atoms to extend the two dimensional crystal in the lateral direction. By following the *in situ* sequential reaction to produce WS_2 and WSe_2 without exposing the product to ambient conditions, the WS_2 peripheral edges remain activated and available for lateral epitaxial growth of WSe_2.

The resulting WS_2-WSe_2 lateral heterostructure domains mostly exhibit a well-faceted equilateral triangular geometry (Fig. 6.2a, b). To probe the spatial structural and optical modulation in WS_2-WSe_2 heterostructures, we have conducted Raman and photoluminescence (PL) studies using a confocal Raman microscope. Importantly, the Raman spectra (excited by 50 μW 514 nm laser) taken from the center and the peripheral regions of a triangular domain clearly show distinct features. The Raman spectrum from the center region show two prominent peaks at 415 cm^{-1} and 358 cm^{-1} (purple line in Fig. 6.2g), corresponding to the A_{1g} and E^1_{2g} resonance modes of WS_2;[42,43] while the Raman spectrum from the peripheral region show a single peak at 255 cm^{-1} (yellow line in Fig. 6.2g), in agreement of the A_{1g} resonance mode of WSe_2.[42,43] These Raman studies demonstrate the co-existence of two distinct materials within the same triangular domain. The Raman mapping studies can further reveal the spatial modulation within the triangular domain, with the central part consisting a smaller triangular domain of WS_2 (Fig. 6.2h), and the peripheral region made of WSe_2 (Fig. 6.2i). A composite Raman mapping image shows seamless lateral integration of WS_2 and WSe_2 in the heterostructure domain (Fig. 6.2j). Similarly, PL studies also show highly distinct PL peaks at ~638 nm for the center part and ~704 nm for the peripheral part (Fig. 6.2c), consistent with the near band edge emission from WS_2 and WSe_2, respectively[20,42,43]. The PL mapping studies (Figs. 6.2 c-f) show similar features to that of Raman

mapping studies, further confirming the formation of WS_2-WSe_2 lateral heterostructures. Importantly, these Raman and PL mapping studies indicate that there is no apparent overlap or gap between WS_2 signal and WSe_2 signal (within the limit of optical resolution), suggesting that WS_2 inner triangle and WSe_2 surrounding areas are laterally connected, although the sharpness of the lateral heterostructures can not be accurately determined based on these optical studies.

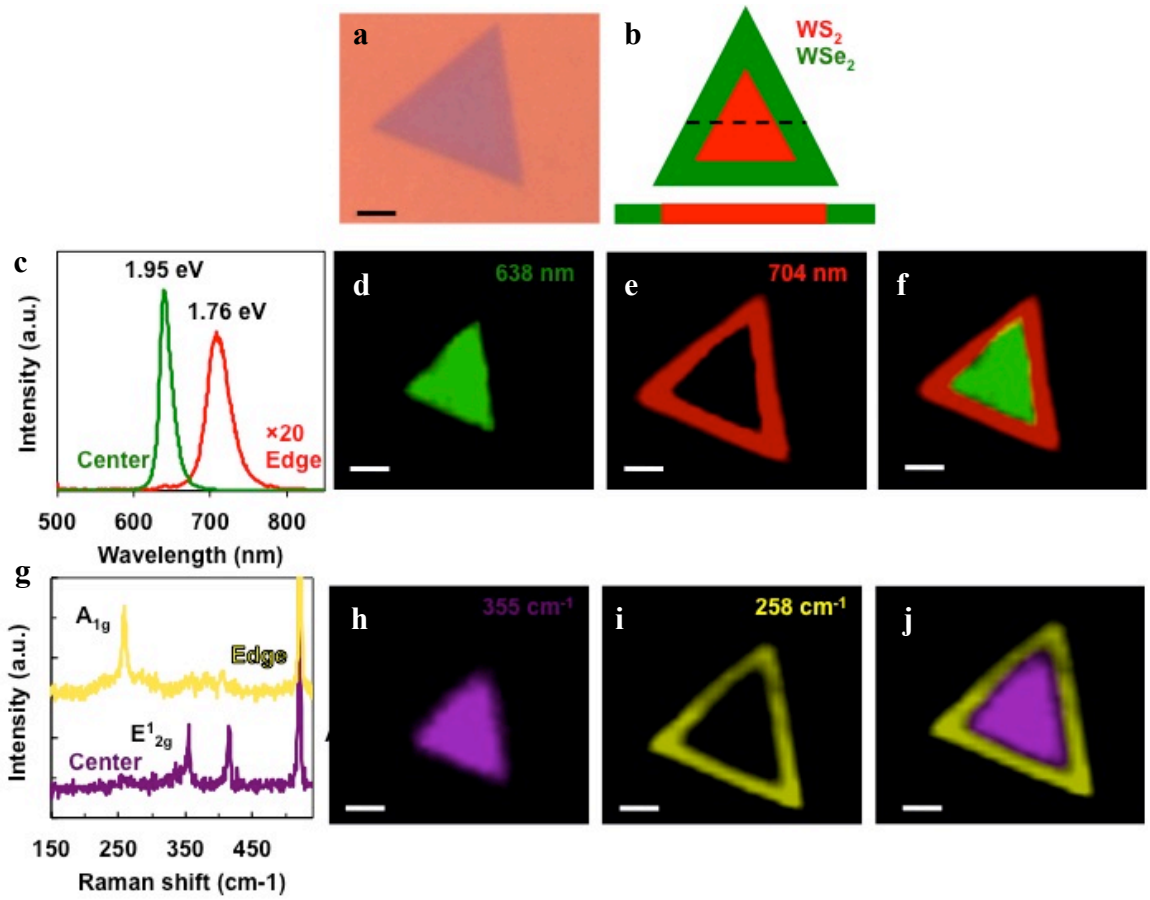

Figure 6.2. (a) An optical micrograph image of a WS_2-WSe_2 heterostructure. **(b)** Schematic diagram the WS_2-WSe_2 regions in the lateral heterostructure. **(c)** Photoluminescence (PL) spectrum of (a) displaying the center and edge regions with emission corresponding to WS_2 and WSe_2, respectively. **(d)** PL map showing the center WS_2 region at 638 nm. **(e)** PL map showing the edge WSe_2 region at 704 nm. **(f)** Overlap of the WS_2 and WSe_2 PL maps. **(g)** Raman spectrum of (a) showing the vibration modes at the center and edge, which correspond to WSe_2 and WS_2, respectively. **(h)** Raman spectra map showing the E_{2g} vibrational mode of WS_2 at 355 cm^{-1}. **(i)** Raman spectra map showing the A_{1g} vibrational mode of WSe_2 at 258 cm^{-1}. **(j)** Overlap of the WS_2 and WSe_2 Raman maps. All scale bars are 2 μm.

6.3 MoS_2-$MoSe_2$ lateral heterostructures

To assess further the generality of the lateral epitaxy strategy for other 2D heterostructures, MoS_2-$MoSe_2$ lateral heterostructure nanosheets have been synthesized using a similar strategy. The MoS_2-$MoSe_2$ lateral heterostructures were grown using MoO_3, S and Se powder as the solid source precursors, in which the vapor phase S first reacting with the MoO_3 to form MoS_2 domains followed by the introduction of Se for successive epitaxial growth of $MoSe_2$ (Fig. 6.1b). It is also noted that MoS_2-$MoSe_2$ can only be obtained when S and Se vapor are switched *in situ* without exposing the MoS_2 nuclei to the ambient conditions. An optical microscope image of a representative MoS_2-$MoSe_2$ lateral heterostructure domain show well-faceted triangular geometry (Fig. 6.3a, inset). AFM studies show a flake thickness of 0.8 nm, indicating a monolayer structure (Fig. 6.3a).

The Raman spectrum taken at the center region show characteristic resonance peaks of monolayer MoS_2, with the out-of-plane A_{1g} mode at 403 cm^{-1} and the in-plane E^1_{2g} mode at 382 cm^{-1} (Fig. 6.3b). These values are slightly red-shifted than those of other CVD grown MoS_2, which might be attributed to slight alloy formation with Se atoms[35,36]. The Raman spectrum taken in the peripheral region show clear peaks at 235 cm^{-1} and 285 cm^{-1}, corresponding to the out-of-plane A_{1g} mode the in-plane E^1_{2g} mode of $MoSe_2$ (Fig. 6.3c). It is also noted that there is an additional peak at 251 cm^{-1} adjacent to the A_{1g} mode of $MoSe_2$, which corresponds slightly S alloyed $MoSe_2$ and is consistent with previous reports[35,36]. Raman mapping at 403 cm^{-1} clearly shows MoS_2 signal is localized to the center triangle (Fig. 6.3d), and the mapping at 235 cm^{-1} demonstrates that $MoSe_2$ signal is only present in the outer peripheral of the triangular heterostructure domain (Fig. 6.3e). PL spectra taken in the center and peripheral regions show characteristic emission peaks corresponding to the near band edge emission of monolayer MoS_2

(680 nm) and monolayer $MoSe_2$ (790 nm) (Fig. 6.3c)[3,4,20]. The MoS_2 emission is slightly red-shifted compared to the reported PL emission from exfoliated one (653-660 nm)[3,4], which may be attributed slight alloy formation (~10%), consistent with previous reports of $MoS_{2-2x}Se_{2x}$ alloys[35,36]. PL maps of MoS_2 at 680 nm (Fig. 6.3f) and $MoSe_2$ at 790 nm (Fig. 6.3g) further confirm the formation of lateral heterostructure across the triangular domain.

The crystallinity of the MoS_2-$MoSe_2$ heterostructures was also examined using transmission electron microscopy (TEM) (Fig. 6.3h) and SAED. The selected area electron diffraction (SAED) patterns taken from either side of MoS_2-$MoSe_2$ heterostructure interface display a typical 6-fold symmetry with the same spatial arrangement and the same spatial orientation (Figs. 6.3i, j). Analysis of the SAED patterns yields lattice spacings of 2.70 Å and 0.278 Å, corresponding to the (100) lattice planes of the MoS_2 and $MoSe_2$ crystal structures, respectively[44]. Lastly, the EDS line scans of S and Se distribution clearly show opposite modulation of S and Se atoms across the MoS_2-$MoSe_2$ heterostructure interface (Fig. 6.3k), with an interface transition over a length scale of ~40 nm (comparable to that of WS_2-WSe_2 heterostructure interface). These studies confirm the formation of MoS_2-$MoSe_2$ lateral heterostructures within the monolayer nanosheet.

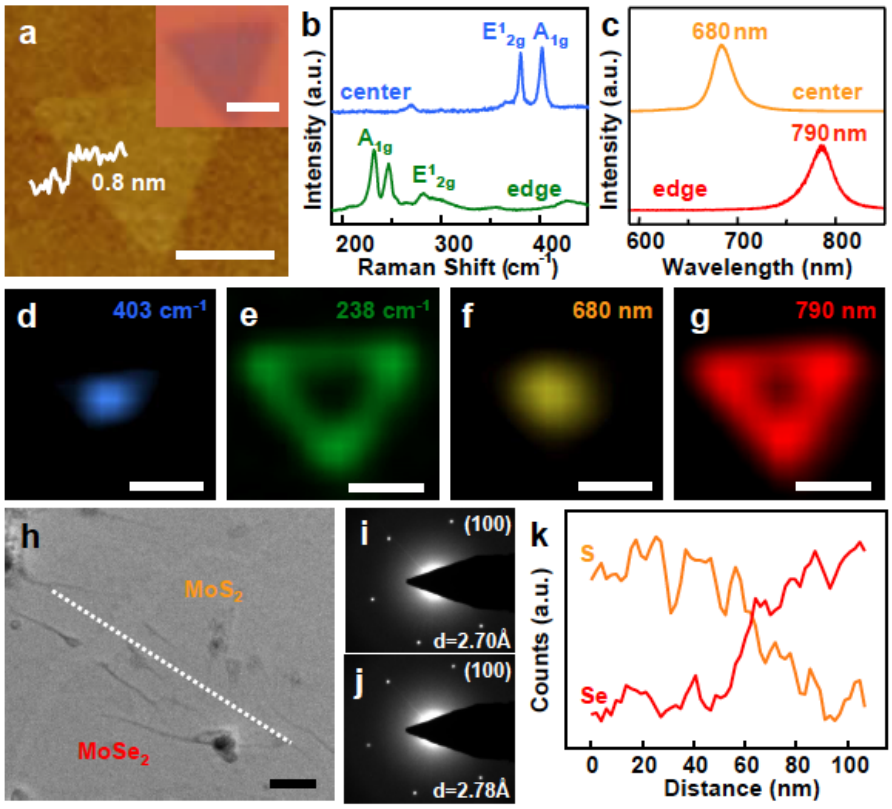

Figure 6.3. (a) AFM and optical microscope image (inset) of a triangular MoS_2-$MoSe_2$ monolayer domain, with an AFM line scan indicating the step height of ~0.8 nm. The scale bars are 2 µm. **(b)** Raman spectra taken from the center (MoS_2) and peripheral area ($MoSe_2$) of a triangular heterostructure domain. **(c)** PL emission spectra obtained from the center (MoS_2) and peripheral area ($MoSe_2$) of a triangular heterostructure domain. (**d**, **e**) Raman spectroscopy maps of the A_{1g} mode of MoS_2 at 403 cm^{-1} (d) and A_{1g} mode of $MoSe_2$ at 235 cm^{-1} (e). The scale bars are 2 µm. (**f, g)** PL maps of the center MoS_2 region with emission at 680 nm (f) and the outer $MoSe_2$ region with emission at 790 nm (g). The scale bars equals to 2 µm. (**h**) Low-resolution TEM image of a monolayer heterostructure nanosheet. The white doted line roughly illustrates the boundary between MoS_2 and $MoSe_2$. The scale bars equals to 200 nm. (**i**, **j**) SAED patterns taken from the MoS_2 region (i) and the $MoSe_2$ region (j) of a lateral heterostructure. (**k**) EDS line scan across the MoS_2-$MoSe_2$ heterostructure interface demonstrates the opposite modulation of S and Se concentration.

6.4 WS_2-WSe_2 vertical heterostructures

Vertical WS_2-WSe_2 heterostructures were grown under the same experimental conditions as the lateral WS_2-WSe_2 heterostructures. Both lateral and vertical heterostructures coexist on the same substrate growth. The synthesized vertical WS_2-WSe_2 heterostructure comprises just two

layers. The underlying WS_2 is typically an equatorial triangular and has larger area compared the top WSe_2 nanosheet. An optical micrograph shows the typical WS_2-WSe_2 vertical heterostructure grown directly on the substrate (Fig. 6.4a). The top WSe_2 layer is triangular and has orientation either parallel or anti-parallel with the underlying WS_2 layer, suggesting an existing epitaxial relationship between WS_2 and WSe_2. The parallel or anti-parallel orientation corresponds to a 60° rotation of a trigonal prismatic crystal structure, consistent with the AA' stacking model of 2H WS_2 and WSe_2. Isolated WSe_2 crystals were not observed on the substrate, indicating all nucleation and growth of WSe_2 crystals occurred exclusively WS_2 monolayer.

Raman spectroscopy and PL measurements were taken on three distinct areas; the peripheral edge of the first layer (region three), the area between the edge of the first layer and the edge of the secondary layer (region two) and the secondary layer region (region one) (Fig. 6.4d, g). The Raman spectrum taken at region two shows the prominent peaks of the WS_2, the A_{1g} resonance mode at 415 cm^{-1} and the E_{2g} resonance mode at 355 cm^{-1} (green line, Fig. 6.4g). The Raman spectrum taken at region one shows the Raman vibrational modes of WS_2 at 415 cm^{-1} (A_{1g}) and 354 cm^{-1} (E_{2g}) and WSe_2 at 251 cm^{-1} (A_{1g}) are present, indicating the presence of a heterojunction interface (black line, Fig. 6.4g). Interestingly, the Raman spectrum fixated on region three shows only a WSe_2 peak at 258 cm^{-1} (A_{1g}), signifying WSe_2 grew on both the peripheral edges and top of the underlying WS_2 nanosheet (orange line, Fig. 6.4g). PL can distinguish between monolayer, bilayer and multilayer WS_2 and WSe_2. PL measured on region two has intense emission at 635 nm (1.95 eV), indicative of WS_2 monolayer direct optical band gap (orange line, Fig. 6.4 d). When PL was measured at the heterojunction in region one, significantly relaxed emission corresponding to WS_2 (635 nm, 1.95 eV) and WSe_2 (705 nm, 1.76 eV) was observed, indicating the double-layer reduced emission and the primary electronic

structure is lower-energy indirect band gap (black line, Fig. 6.4d). Interestingly, when PL was measured at region three, enhanced emission at 705 nm (1.76 eV) was observed, indicative of monolayer WSe_2 (red line, Fig. 6.4d). AFM measurements on the vertical heterostructure show a ~0.7 nm jump from the substrate to the crystal (Fig. 6.4b). The height scan from the monolayer region to the heterojunction region shows the jump to be ~0.9 nm, confirming the heterojunction region is one layer thick. The combined results of Raman, PL and AFM indicate the presence of both lateral and vertical WS_2-WSe_2 heterojunction interfaces within the crystal (representative schematic in Fig. 6.4c)

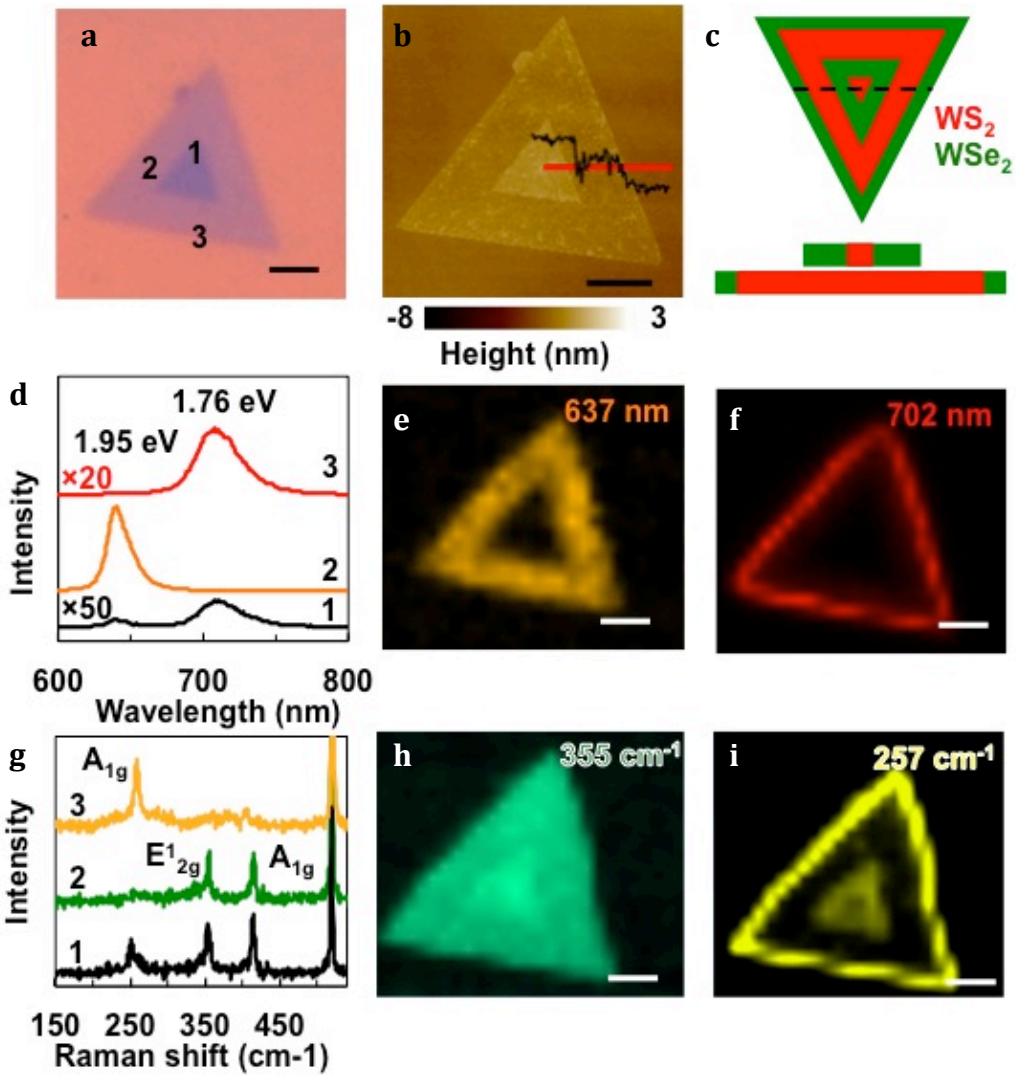

Figure 6.4 (a) An Optical micrograph of a vertical WS_2-WSe_2 heterostructure. **(b)** Atomic force micrograph of (a). The height from the bilayer and monolayer are ~0.9 and~ 0.7 nm, respectively. **(c)** Illustration showing the WS_2 and WSe_2 regions of (a). **(d)** PL spectrum depicting emission from regions one, two and three from the optical micrograph in (a). **(e)** PL map of WS_2 focused at 637 nm. **(f)** PL map of WSe_2 focused at 702 nm. **(g)** Raman spectrum depicting vibrational modes from regions one, two and three. **(g)** Raman map highlighting WS_2 E_{2g} vibrational mode at 355 cm^{-1}. WS_2 encompasses the entire crystal **(h)** Raman map highlighting the WSe_2 A_{1g} vibrational mode at 257 cm^{-1}. WSe_2 is located at the bilayer and edge of the crystal. All scale bars are 2 μm.

6.5 MoS_2-$MoSe_2$ vertical heterostructures

Akin to WS_2-WSe_2 heterostructures, vertical MoS_2-$MoSe_2$ heterojunctions grew alongside the lateral MoS_2-$MoSe_2$ heterostructure counterparts. During the MoS_2 growth process, some MoS_2 sheets grew into films with lateral areas of 100 μm x 100 μm, similar to MoS_2 films reported in chapter 2 (Fig. 2.2f). Darker $MoSe_2$ triangular heterojunctions were found on top of the MoS_2 film with lateral lengths up to several tens of μm. The $MoSe_2$ crystals were aligned parallel or antiparallel to one another, indicating an epitaxial relationship between the MoS_2 and $MoSe_2$. On each film, there were several clusters of $MoSe_2$ heterobilayers (Fig. 6.5a). A darker optical contrast exists between the $MoSe_2$ heterobilayer and the MoS_2 homobilayer (Fig 6.5a, b), due to larger absorption coefficient for $MoSe_2$ compared to MoS_2.[46]

Raman and PL spectroscopies were implemented to probe the optical and vibrational MoS_2-$MoSe_2$ vertical heterostructure. Raman spectroscopy measurements focused on the underlying film show peaks at 404 cm^{-1} and 387 cm^{-1}, indicative of the A_{1g} and E_{2g} resonance modes of monolayer MoS_2 (blue line, Fig. 6.5g). The Raman spectrum taken at the triangular bilayer region displays two distinctive sets of peaks. The first peak is at 239 cm^{-1}, which correspond to the A_{1g} of $MoSe_2$, while the peaks at 387 cm^{-1} and 404 cm^{-1} match with the peaks of region one, indicating the MoS_2 film lies beneath the $MoSe_2$ layer (pink like, Fig. 6.5g). Raman mapping clearly distinguishes the MoS_2 film (blue region, Fig. 6.5h) from the MoS_2-

$MoSe_2$ heterojunctions (maroon triangles, Fig. 6.5i). PL emission intensity can distinguish single and multilayers within a MoS_2 or $MoSe_2$ nanosheet. PL emission spectroscopy taken on the underlying film display intense emission at 680 nm (1.82 eV), confirming the film is monolayer MoS_2 (black line, Fig. 6.5d). PL emission spectroscopy focused on the bilayer region has significantly relaxed emission located at 680 nm (1.82 eV) and 805 nm (1.54 eV), corresponding to MoS_2 and $MoSe_2$, respectively (red line, Fig. 6.5d). The bilayer emission observed corresponds to the direct band gap electronic pathway of MoS_2 and $MoSe_2$, except with significantly reduced intensity compared to its monolayer counterpart. PL mapping highlights the distinguishing divisions between MoS_2 film (yellow region, Fig. 6.5e) and the MoS_2-$MoSe_2$ vertical heterojunction (white triangles, Fig. 6.5f). The black voids on the MoS_2 PL map show the clear difference in emission intensity between the MoS_2 film and the MoS_2-$MoSe_2$ heterojunctions. The combined results of Raman and PL spectroscopies show that the vertical heterostructure consists of an underlying MoS_2 film and a secondary $MoSe_2$ nanosheet.

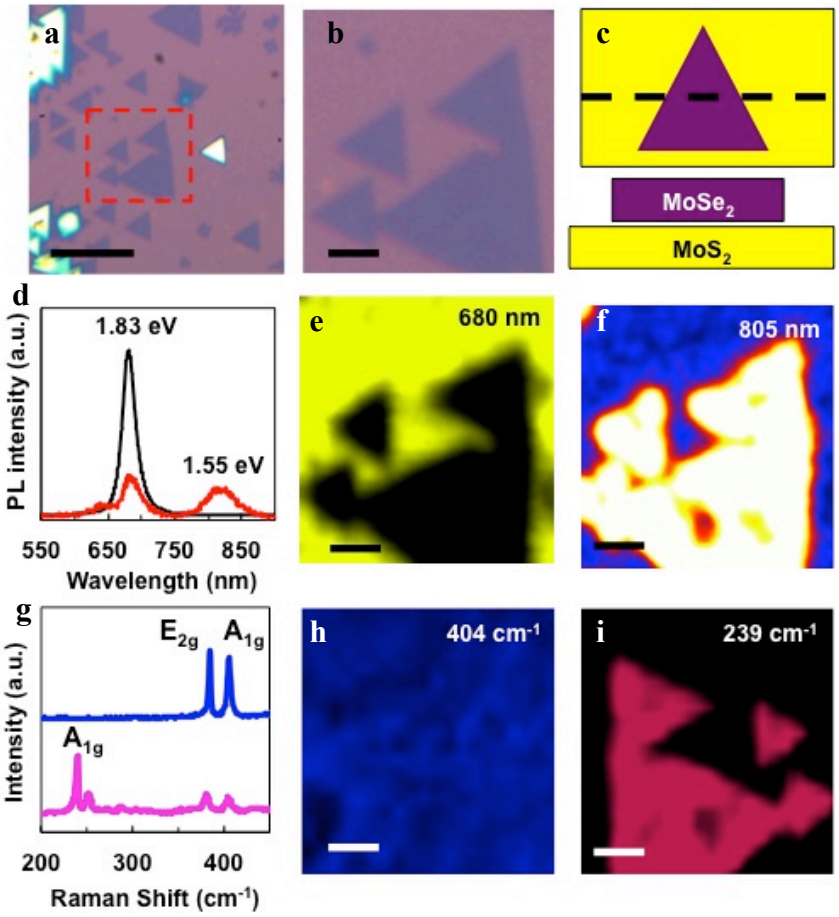

Figure 6.5. (a) An Optical micrograph of a vertical MoS_2-$MoSe_2$ heterostructures. The underlying film is MoS_2. The secondary thin and thick crystals are $MoSe_2$. The scale bar is 6 μm. **(b)** Enhanced image of (a) highlighting several heterojunctions of interest. **(c)** Top-down and cross-section schematic showing the composition of the heterojunction in (a, b). **(d)** PL spectrum depicting emission from the MoS_2 underlying film (black line) and from the $MoSe_2$-MoS_2 heterojunction (red line) **(e)** PL map of MoS_2 focused at 680 nm. **(f)** PL map of $MoSe_2$ focused at 702 nm. **(g)** Raman spectrum depicting acoustic vibrations from the MoS_2 underlying film (blue line) and the MoS_2-$MoSe_2$ heterojunction (pink line). **(g)** Raman map highlighting MoS_2 A_{1g} vibrational mode at 404 cm^{-1}. MoS_2 encompasses the entire image **(h)** Raman map highlighting the $MoSe_2$ A_{1g} vibrational mode at 239 cm^{-1}. $MoSe_2$ is confined to the heterojunction. All scale bars (except Fig 6.5a) are 2 μm.

6.6 Heterostructure growth mechanism

Since both the vertical and lateral MoS_2-$MoSe_2$ and WS_2-WSe_2 heterostructures exist on the same substrate, there must be some difference in morphology that promotes the selective growth of either vertical or lateral heterostructures. $MoSe_2$ bilayers have a darker optical contrast

compared to MoS_2 bilayers due to the larger absorption coefficient of $MoSe_2$.[46] Focusing first on MoS_2-$MoSe_2$, select OM images reveal an optical contrast within the bilayer of the heterojunction (Fig. 6.6a). To show that the regions optical contrast is not due to fluctuations in nanosheet thickness, an atomic force micrograph shows the height of the bilayer region does not vary (Fig. 6.6b). Regions one, two, and three on the OM and AFM images show monolayer MoS_2, bilayer MoS_2 and heterostructured MoS_2-$MoSe_2$, respectively. PL measurements taken on the bilayer (region two) show mild emission at 680 nm (green line, Fig. 6.6d), while the underlying MoS_2 film region has intense emission at 680 nm (blue line, Fig. 6.6d), corresponding to bilayer and monolayer MoS_2, respectievly.[3,4] The outer region heterojunction has trivial emission at 680 nm and stronger emission at 800 nm (red line, Fig. 6.6d), consistent with previous MoS_2-$MoSe_2$ vertical heterojunction PL emission spectroscopy. The PL map highlights the difference between MoS_2 (680 nm, Fig. 6.6e) and $MoSe_2$ (800 nm, Fig. 6.6f). The Raman spectrum in region one (blue line, Fig. 6.6g) shows characteristic MoS_2 vibrational modes at 403 cm^{-1} (A_{1g}) and 380 cm^{-1} (E2g). The Raman spectrum in region two (green line, Fig. 6.6g) has intense vibrational peaks at 403 cm^{-1} (A_{1g}) and 375 cm^{-1} (E_{2g}). The peaks in region three (red line, Fig. 6.6g) have peaks at 239 cm^{-1} ($MoSe_2$ A_{1g}), 401 cm^{-1} (MoS_2 A_{1g}) and 379 cm^{-1} (MoS_2 E_{2g}). The $MoSe_2$ region is emphasized in the Raman map, and has a noticeable hexagonal void in the center where the MoS_2 homobilayer resides (Fig. 6.6i). It is worth noting that the lack of $MoSe_2$ Raman signature in region two, as well as the larger MoS_2 resonance intensity in region one is well-defined in the MoS_2 Raman map (Fig. 6.6h). The combined OM and AFM images, Raman and PL spectra and maps confirm the crystal consists of an underlying MoS_2 film, with a MoS_2 homobilayer that is laterally stitched to a $MoSe_2$ heterobilayer. Essentially, both vertical and lateral heterojunctions exist within the same crystal. Although this mechanism was observed for

many of the MoS_2-$MoSe_2$ vertical heterostructures, some of the vertical heterostructures didn't conclusively show a homobilayer (Fig. 6.5). Since MoS_2 is reported to nucleate and grow on rough surfaces, this can help induce heterogeneous nucleation in the underlying surface. However, most of the heterostrucutres observed follow the homobilayer formation.

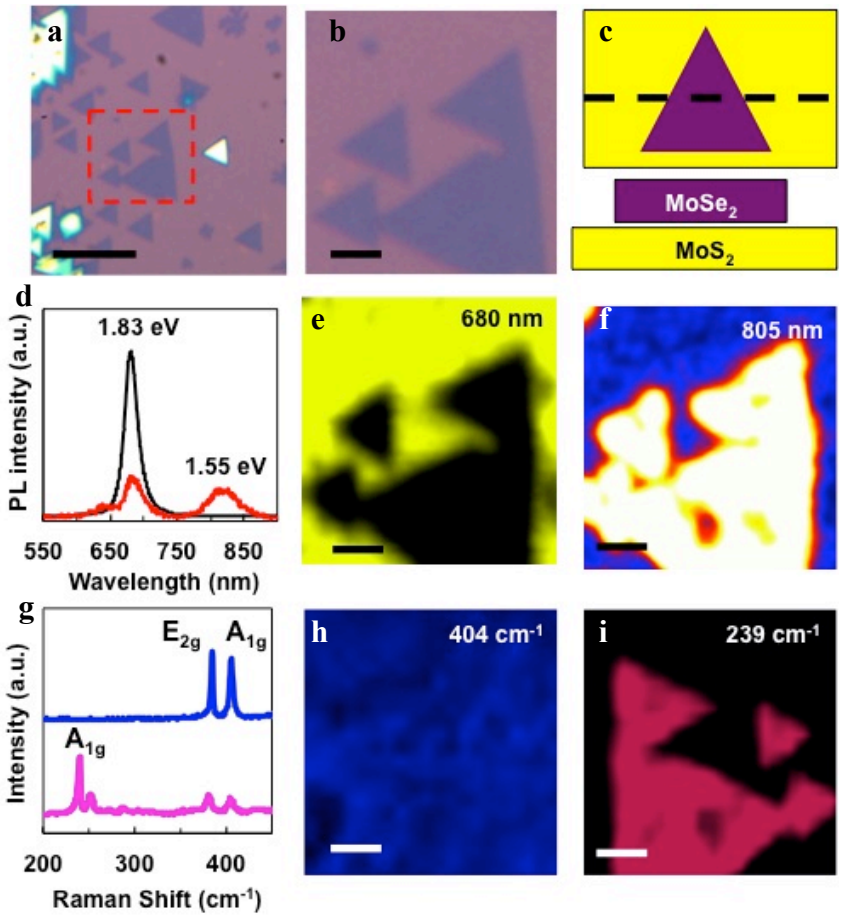

Figure 6.6. (a) Optical micrograph of a MoS_2-$MoSe_2$ vertical heterostructure. Regions one, two and three correspond to monolayer MoS_2, bilayer $MoSe_2$ and heterostructured MoS_2-$MoSe_2$, respectively. **(b)** AFM image of (a) showing the basal plane of the crystal is flat across the interface between region two and three. **(c)** Illustration displaying the top-down and cross-section of image (a). **(d)** Photoluminescence (PL) spectrum showing region one (MoS_2, blue line), region two (MoS_2, 10x enhanced green line), and region three (MoS_2-$MoSe_2$ heterojunction, red line). **(e)** PL map focused at 680 nm (MoS_2). **(f)** PL map focused at 800 nm ($MoSe_2$). **(g)** Raman spectrum showing region one (MoS_2, blue line), region two (MoS_2, green line), and region three (MoS_2-$MoSe_2$ heterojunction, red line). **(h)** Raman map depicting the MoS_2 regions (A_{1g}, 403 cm^{-1}). (i) Raman map depicting the $MoSe_2$ regions (A_{1g}, 239 cm^{-1}).

WS_2-WSe_2 vertical heterostructures were examined to determine the vertical heterostructure formation mechanism (Fig. 6.7a). The phase mode of AFM can be used to highlight the differences in surfaces due to the stiffness between the tip and the crystal surface. Hence, it can distinguish between WS_2 and WSe_2 surfaces in an AFM image. When a phase AFM image was generated on a vertical WS_2-WSe_2 heterostructure, clear differences in the composition of a vertical heterostructure are noticed (Fig. 6.7c). An AFM height scan of the same WS_2-WSe_2 crystal shows the height difference from the substrate to the nanosheet is 0.7 nm, and across the bilayer is ~0.9 nm (Fig. 6.7b). The height is level across the monolayer and bilayer region. From the AFM study, the WS_2-WSe_2 crystal is divided into four sections; region one at the center of the crystal, region two the bilayer area surrounding area region one, region three the underlying monolayer crystal and region four, the peripheral monolayer area surrounding area region three. Raman and PL spectra and maps confirm that regions one and three consist of bilayer and monolayer WS_2, while regions two and four consist of monolayer WSe_2 (Fig. 6.4). From the combined results of AFM, Raman and PL, the crystal is revealed to have a WS_2 monolayer and homobilayer, and two independent WSe_2 heterojunctions at thebilayer and monolayer interfaces. For crystals with an absence of a homobilayer, only lateral WS_2-WSe_2 heterostructures are observed.

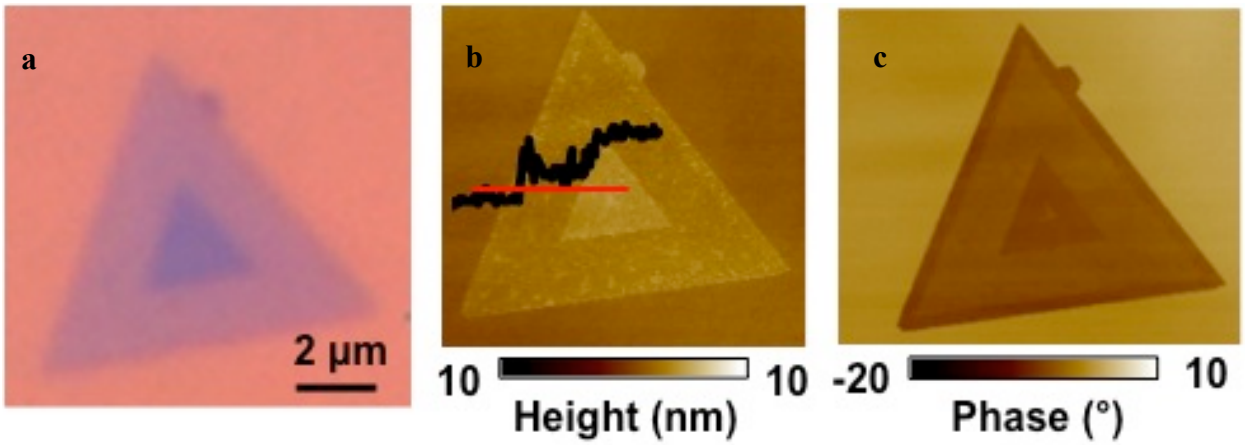

Figure 6.7 (a) An optical micrograph of a vertical WS_2-WSe_2 heterostructure. **(b)** Atomic force micrograph of (a) showing the height difference between the substrate and the center region is ~0.7 and ~0.9 nm. There is no appreciable height difference between the WS_2 and WSe_2 within the heterojunction. **(c)** Phase image showing a contrast between WS_2 (lighter) and WSe_2 (darker) surfaces on the crystal.

From the observations of a homobilayer presence on both MoS_2-$MoSe_2$ and WS_2-WSe_2 vertical heterostructures, a growth mechanism explanation emerges. After the initial underlying layer is created, the MoS_2 or WS_2 nanosheets either consist of a smooth basal plane or have a homobilayer. After the Se precursors are introduced, $MoSe_2$ or WSe_2 only grows at high-energy interfaces. It is known that the edges of MoS_2 or WS_2 consist of dangling S or Mo bonds, whereas the basal plane of MoS_2 and WS_2 has completely saturated bonds. Consequently, the $MoSe_2$ preferentially grows on these exposed MoS_2 lateral edges. In the absence of a homobilayer of MoS_2 or WS_2, the $MoSe_2$ or WSe_2 lacks the required energy to nucleate and create a new surface on the underlying basal plane. Therefore, whenever a homobilayer exists, the secondary grown $MoSe_2$ or WSe_2 will grow into a vertical heterostructure. However, in the absence of a homobilayer, the secondary grown $MoSe_2$ or WSe_2 will grow only into a lateral $MoSe_2$ or WSe_2 heterojunction. These observations match a growth mechanism study of single and multilayered MoS_2 describing the probability of precursors growing at the crystal edges rather than the basal plane.[47]

6.7 Conclusion

In summary, we have successfully demonstrated the growth of lateral heterojunctions of 2-D layered semiconductors through a hetero-epitaxial approach. The realization of lateral heterojunction in the 2-D layered semiconductors can open up exciting opportunities for creating a wide range of functional devices, ranging from the complementary logic circuits, photovoltaics, photo-detectors, to light-emitting diodes and laser diodes. Lateral MoS_2-$MoSe_2$ and WS_2-WSe_2 had a laterally stitched epitaxial interface characterized by optical microscopy, atomic force microscopy, transmission electron microscopy, Raman and photoluminescence spectroscopy. Vertical MoS_2-$MoSe_2$ and WS_2-WSe_2 heterostuctures consisted of an underlying "S" based transition metal dichalcogenide layer and an "Se" based secondary layer, confirmed by optical microscopy, atomic force microscopy, Raman and photoluminescence spectroscopy. Vertical heterostructures were found to grown when a homobilayer of the "S" based transition metal dichalcogenide grew. From the dangling bond at the peripheral edges of the vertical heterostructure (terminal bilayer and monolayer regions), the $MoSe_2$ or WSe_2 grew into extended 2-D sheets. In the absence of a MoS_2 or WS_2 homobilayer formation, only lateral heterostructures were observed.

6.8 Method Summary

6.8.1 MoS_2-$MoSe_2$ heterostructures

The MoS_2 was grown similarly to the chapter 2 method. 0.1 g MoO_3 powder (Sigma, 99.9%) was placed in a 5 mL alumina boat in quartz tube in the center of the heating zone in a 12-inch horizontal tube furnace (Lindberg Blue). 0.08 g of S powder (Sigma, 99.9%) and 0.3 g of Se powder (Sigma, 99.9%) were placed in upstream of the MoO_3 boat. Three substrates were placed polished-side-down on top of the MoO_3 boat packed tightly together. 100 standard cubic

centimeters (sccm) of Ar was flowed through the tube and purged under vacuum several times. The pressure was maintained at 1 atm throughout the reaction. The furnace was ramped at 50 °C/min until reaching the growth temperature of 750 °C. The tube was then shifted to place the S powder at the edge of the furnace to supply sufficient heating for to vaporize the S powder. The S powder was sufficiently vaporized in five minutes and the furnace temperature was lowered to 700 °C. After several minutes, the furnace reached 700 °C and 5 sccm of H_2 was flowed alongside 65 sccm of Ar gas in order to promote the $MoSe_2$ growth. Immediately after activating H_2 gas, the Se powder was placed in the heating region (similar location as the S was in the prior growth) and the Se powder was allowed to vaporize for fifteen minutes. After fifteen minutes, the furnace was turned off and allowed to cool to room temperature. When the furnace cooled to room temperature, the substrates were removed and characterized.

6.8.2 WS_2-WSe_2 heterostructures

The WS_2 was grown first similar to the previously reported method in chapter 3. 0.01 g was spread out on the substrate, which was placed slightly before the center of the furnace. Three 2 cm× 2 cm silicon oxide substrates were placed downstream 1 cm away from the substrate containing WO_3, and 1 cm apart from each other substrate. 100 sccm of Ar was flowed through the tube and purged under vacuum several times. The pressure was maintained at 1 atm throughout the reaction. The furnace was heated at 50 °C/min until reaching the growth temperature of 850 °C. The tube was then moved 1 - 2 cm into the heating zone to place the S powder at the edge of the furnace. After five minutes when the S powder was sufficiently vaporized, 5 sccm of H_2 was flowed order to enhance the WSe_2 growth. After activating the H_2 flow, Se powder was immediately placed in the heating region and the Se powder was allowed to

vaporize. After fifteen minutes, the furnace was turned off and allowed to cool to room temperature for characterization.

6.8.3 Characterizations.

The microstructures and morphologies of the nanostructures are characterized by optical microscope, atomic force microscope (AFM), and transmission electron microscope (TEM). The micro-Raman and micro-PL studies were conducted using a Horiba LABHR confocal Raman system with an Ar ion laser (514 nm) excitation.

6.9 References

(1) Novoselov, K. S. *et al.* Two-dimensional atomic crystals. *Proc. Natl Acad. Sci. USA* **102**, 10451-10453 (2005).

(2) Mak, K. F., Lee, C., Hone, J., Shan, J. & Heinz, T. F. Atomically thin MoS_2: A new direct-gap semiconductor. *Phys. Rev. Lett.* **105**, 136805 (2010).

(3) Splendiani, A. *et al.* Emerging photoluminescence in monolayer MoS_2 *Nano Lett.* **10**, 1271-1275 (2010).

(4) Eda, G. *et al.* Photoluminescence from chemically exfoliated MoS_2. *Nano Lett* **11**, 5111-5116(2011).

(5) Radisavljevic, B., Radenovic, A., Brivio, J., Giacometti, V. & Kis, A. Single-layer MoS_2 transistors. *Nat. Nanotechnol.* **6**, 147-150 (2011).

(6) Wang, Q. H., Kalantar-Zadeh, K., Kis, A., Coleman, J. N. & Strano, M. S. Electronics and optoelectronics of two-dimensional transition metal dichalcogenides. *Nat. Nanotech.* **7**, 699-712 (2012).

(7) Geim, A. K. & Grigorieva, I. V. Van der Waals heterostructures. *Nature* **499**, 419-425 (2013).

(8) Chhowalla, M. *et al.* The chemistry of two-dimensional layered transition metal dichalcogenide nanosheets. *Nat. Chem.* **5**, 263-275 (2013).

(9) Huang, X.; Zeng, Z. Y. & Zhang, H. Metal dichalcogenide nanosheets: preparation, properties and applications. *Chem. Soc. Rev*. **42**, 1934-1946 (2013).

(10) Britnell, L. *et al.*Field-effect tunneling transistor based on vertical graphene heterostructures. *Science* **335**, 947-950 (2012).

(11) Yu W. J. *et al.* Vertically stacked multi-heterostructures of layered materials for logic transistors and complementary inverters. *Nat. Mater.* **12**, 246-252 (2013).

(12) Roy, K. *et al.*Graphene-MoS_2 hybrid structures for multifunctional photoresponsive memory devices. *Nat. Nanotechnol.* **8**, 826-830 (2013).

(13) Britnell, L. *et al.*Strong light-matter interactions in heterostructures of atomically thin films. *Science* **340**, 1311-1314 (2013).

(14) Yu W. J. *et al.* Highly efficient gate-tunable photocurrent generation in vertical heterostructures of layered materials. *Nat. Nanotechnol.* **8**, 952-958 (2013).

(15) Mak, K. F. *et al.*Ultrasensitive photodetectors based on monolayer MoS_2. *Nat. Nanotechnol.* **8**, 497-501 (2013).

(16) Jones, A. M. *et al.*Spin-layer locking effects in optical orientation of exciton spin in bilayer WSe_2. *Nat. Phys.* **10**, 130-134 (2014).

(17) Sundaram, R. S. *et al.*Electroluminescence in single layer MoS_2. *Nano Lett.* **13**, 1416-1421 (2013).

(18) Baugher, B. W. H., Churchill, H. O. H., Yang, Y. & Jarillo-Herrero, P. Optoelectronic devices based on electrically tunable p-n diodes in a monolayer dichalcogenide. *Nat. Nanotechnol.* **9**, 262-267 (2014).

(19) Pospischil, A., Furchi, M. M., Mueller, T. Solar-energy conversion and light emission in an atomic monolayer p-n diode. *Nat. Nanotechnol.* **9**, 257–261 (2014).

(20) Ross, J. S. *et al.*Electrically tunable excitonic light-emitting diodes based on monolayer WSe_2 p-n junctions. *Nature Nanotechnol.* **9**, 268-272 (2014).

(21) Lopez-Sanchez, O. *et al.* Light generation and harvesting in a van der Waals heterostructure. *ACS Nano* **8**, 3042-3048 (2014).

(22) Zhang, Y., Oka, T., Suzuki, R., Ye, J. & Iwasa, Y. Electrically switchable chiral light-emitting transistor. *Science* **344**, 725-728 (2014).

(23) Levendorf, M. P. *et al.* Graphene and boron nitride lateral heterostructures for atomically thin circuitry. *Nature* **488,** 627-632 (2012).

(24) Liu, Z. *et al.* In-plane heterostructures of graphene and hexagonal boron nitride with controlled domain sizes. *Nat. Nanotechnol.* **8,** 119-124 (2013).

(25) Lei, L. *et al.* Heteroepitaxial growth of two-dimensional hexagonal boron nitride templated by graphene edges. *Science* **343,** 163-167 (2014).

(26) Jiong, L. *et al.* Order-Disorder Transition in a Two-Dimensional Boron-Carbon-Nitride Alloy, *Nat. Commun.* **4**, 3681 (2013).

(27) Lee, Y. H.*et al.* Synthesis of large-area MoS_2 atomic layers with chemical vapor deposition. *Adv. Mater.* **24**, 2320-2325 (2012).

(28) Liu, K. K. *et al.* Growth of large-area and highly crystalline MoS_2 thin layers on insulating substrates. *Nano Lett.* **12**, 1538-1544 (2012).

(29) Lee, Y. H. *et al.* Synthesis and transfer of single-layer transition metal disulfides on diverse surfaces. *Nano Lett.* **13**, 1852-1857 (2013).

(30) Van der Zande, A. M. *et al.* Grains and grain boundaries in highly crystalline monolayer molybdenum disulphide. *Nat. Mater.* **12***,* 554-561 (2013).

(31) Najmaei, S. *et al.* Vapour phase growth and grain boundary structure of molybdenum disulphide atomic layers. *Nat. Mater.* **12**, 754-759 (2013).

(32) Yu, Y. *et al.* Controlled scalable synthesis of uniform, high-quality monolayer and few-layer MoS_2 films, *Sci. Rep.* **3**, 1866, (2013).

(33) Zhang, Y. *et al.* Controlled growth of high-quality monolayer WS_2 layers on sapphire and imaging its grain boundary. *ACS Nano* **7**, 8963-8971 (2013).

(34) Shaw, J. C. *et al.* Chemical vapor deposition growth of monolayer $MoSe_2$ nanosheets *Nano Res*. **7**, 511-517 (2014).

(35) Mann, J. *et al.* 2-Dimensional transition metal dichalcogenides with tunable direct band gaps: $MoS_{2(1-x)}Se_{2x}$ monolayers. *Adv. Mater.* **26**, 1399–1404 (2014).

(36) Li, H. *et al.* Growth of alloy $MoS_{2x}Se_{2(1-x)}$ nanosheets with fully tunable chemical compositions and optical properties. *J. Am. Chem. Soc.* **136**, 3756-3759 (2014).

(37) Schmidt. H. *et al.* Transport properties of monolater MoS_2 grown by chemical vapor deposition. *Nano. Lett.* **14**, 1909-1913 (2014).

(38) Ling, X. *et al.* Role of the seeding promoter in MoS_2 growth by chemical vapor deposition. *Nano. Lett.* **14**, 464-472 (2014).

(39) Huang, J. K. *et al.* Large-area synthesis of highly crystalline WSe_2 monolayers and device applications. *ACS Nano* **14**, 923-930 (2014).

(40) Tongay, S. *et al.*Two-dimensional semiconductor alloys: monolayer $Mo_{1-x}W_xSe_2$, *Appl. Phys. Lett.*, **104**, 012101 (2014).

(41) Zhou, H. *et al.* Thickness-dependent patterning of MoS_2 sheets with well-oriented triangular pits by heating in air," *Nano Res*. **6**, 703–711 (2013).

(42) Zhao, W. J. *et al.* Evolution of electronic structure in atomically thin sheets of WS_2 and WSe_2. *Acs Nano* **7**, 791-797 (2013).

(43) Gutierrez, H. R. *et al.* Extraordinary room-temperature photoluminescence in triangular WS_2 monolayers. *Nano Lett* **13**, 3447-3454 (2013).

(44) Coehoorn, R. , Dijkstra, C. H., J. & Flipse, C. J. F. Electronic structure of $MoSe_2$, MoS_2, and WSe_2. I. Band-structure calculations and photoelectron spectroscopy. *Phys. Rev. B* **35** 6195-6202 (1987).

(45) Yan, K. *et al.* Modulation-doped growth of mosaic graphene with single-crystalline p–n junctions for efficient photocurrent generation. *Nat. Commun.* **3**, 1280 (2012).

(46) Tonndorf, P. *et al.* Photoluminescence emission and Raman response of monolayer MoS_2, $MoSe_2$, and WSe_2. *Optics Express* **21**, 4908-4916 (2013).

(47) Hanse, L. P. *et al.* Growth Mechanism for Single- and Multi-Layer MoS_2 nanocrystals. *J. Phys. Chem. C.* **118**, 22768-22773 (2014).

Chapter 7. Conclusion

MoS_2, WS_2, $MoSe_2$ and WSe_2, all members of the group six transition metal dichalcogenide family, were synthesized. The transition metal dichalcogenide single and few-layer triangular nanosheets were grown directly onto 300 nm SiO_2/Si substrates. MoS_2, WS_2 and $MoSe_2$ were grown using a combination of S, Se, MoO_3 (H_2 gas with $MoSe_2$) and WO_3 precursors in a chemical vapor deposition apparatus. WSe_2 was grown using an alternative deposition method, where WSe_2 bulk powder was vaporized and grew on substrates located in a cooler region. The single and few-layer transition metal dichalcogenides were optically distinguishable, nucleated randomly on the substrate and had edge lengths up to 100 μm.

For MoS_2, Raman spectroscopy was used extensively not only to verify the crystal structure, but also to highlight differences between bulk and single-layer vibrational modes. Atomic force microscopy showed the thickness of a single layers to be between ~ 0.65 – 1.0 nm. Photoluminescence emission of MoS_2 single layers had an intense emission peak corresponding to the optical direct band gap. Thicker MoS_2 has had significantly reduced emission since the primary electronic pathway is a lower energy indirect band gap. In the case of WS_2, Raman spectroscopy verified the crystal structure and highlighted changes between single and few-layers of the crystals. WS_2 photoluminescence emission probed direct band gap emission of monolayer WS_2, while showing thicker synthesized WS_2 had no direct band gap signature.

Large area $MoSe_2$ nanosheets using MoO_3 and Se powder precursors in a mixture of Ar and H_2 gases in a horizontal tube furnace. H_2 is a critical component of the reaction by enhancing the reduction of MoO_3 with Se to form $MoSe_2$. $MoSe_2$ analyzed using Raman spectroscopy showed a thickness-dependent vibrational shift. Monolayer $MoSe_2$ photoluminescence has intense emission centered 800 nm, corresponding to the optical direct band gap.

An alternative method of vaporizing solid WSe_2 powder to synthesize WSe_2 monolayers, bilayers, and few-layer nanosheets was described. The method utilizes the vaporization of bulk WSe_2 powder, which grows into isolated domains and films at the cooler end of the tube furnace. Through the characterization of atomic force microscopy, photoluminescence, transmission electron microscopy and Raman spectroscopy, we show that the large area monolayer WSe_2 thin film with lateral dimensions approaching ~ 1 cm^2.

Finally, the growth of lateral heterojunctions of 2-D layered semiconductors through a lateral hetero-epitaxial approach is described. The realization of lateral heterojunction in the 2D layered semiconductors can open up exciting opportunities for creating a wide range of functional devices, ranging from the complementary logic circuits, photovoltaics, photodetectors, to light-emitting diodes and laser diodes. Lateral MoS_2-$MoSe_2$ and WS_2-WSe_2 consisted of a laterally stitched epitaxial interface characterized by optical microscopy, atomic force microscopy, transmission electron microscopy, Raman and photoluminescence spectroscopy. Vertical MoS_2-$MoSe_2$ and WS_2-WSe_2 heterostuctures consisted of an underlying "S" based transition metal dichalcogenide layer and a "Se" based secondary layer, confirmed by optical microscopy, atomic force microscopy, Raman and photoluminescence spectroscopy. Vertical heterostructures were found to grown when a homobilayer of the "S" based transition metal dichalcogenide grew. From the dangling bonds at the peripheral edges of the vertical heterostructure (terminal bilayer and monolayer regions), the $MoSe_2$ or WSe_2 grew into extended 2D sheets. In the absence of a MoS_2 or WS_2 homobilayer formation, only lateral heterostructures were observed. My dissertation research has helped shape the field of 2-D semiconducting film research, and the methods described shape the future for 2-D materials synthesis on a grand scale.